Click Here for Full Article

Ocean viscosity and climate

M. Jochum,[1] G. Danabasoglu,[1] M. Holland,[1] Y.-O. Kwon,[1] and W. G. Large[1]

[1] The impacts of parameterized lateral ocean viscosity on climate are explored using three 120-year integrations of a fully coupled climate model. Reducing viscosity leads to a generally improved ocean circulation at the expense of increased numerical noise. Five domains are discussed in detail: the equatorial Pacific, where the emergence of tropical instability waves reduces the cold tongue bias; the Southern Ocean, where the Antarctic Circumpolar Current increases its kinetic energy but reduces its transport; the Arctic Ocean, where an improved representation of the Atlantic inflow leads to a better sea-ice distribution; the North Pacific, where the more realistic path of the Kuroshio leads to more realistic temperatures across the midlatitude Pacific; and the northern marginal seas, where stronger boundary currents lead to significantly less sea-ice. Although the ocean circulation and sea-ice distribution improve, the oceanic heat uptake, the poleward heat transport, and the large scale atmospheric circulation are not changed significantly. In particular, the improvements to the equatorial cold tongue did not lead to better representation of tropical precipitation or El Niño.

Citation: Jochum, M., G. Danabasoglu, M. Holland, Y.-O. Kwon, and W. G. Large (2008), Ocean viscosity and climate, *J. Geophys. Res.*, *113*, C06017, doi:10.1029/2007JC004515.

1. Introduction

[2] Ocean mesoscale eddies have an important impact on the ocean tracer and momentum budgets, but they are not resolved in climate models and hence have to be parameterized. While understanding and parameterizing mesoscale tracer fluxes has a long and fruitful history [e.g., *Solomon*, 1971; *Gent and McWilliams*, 1990; *Visbeck et al.*, 1997; *Griffies*, 2004], the development of a parameterization for eddy momentum fluxes (viscosity hereafter) is hindered by numerous mathematical and numerical challenges [e.g., *Wajsowicz*, 1993; *Gent and McWilliams*, 1996; *Large et al.*, 2001].

[3] Viscosity acts to diffuse momentum and to dissipate energy in numerical models of atmosphere and ocean. It is thought to represent the effect of all unresolved motions and is also necessary to achieve numerical stability. For current Atmospheric General Circulation Models (AGCMs) it is relatively straightforward to determine the appropriate level of viscosity: AGCMs resolve quasi-geostrophic turbulence which can generate upgradient momentum transfer, and downgradient viscosity is chosen so that the wave number spectrum agrees with theoretical expectations and observations [*Boville*, 1991]. In Ocean General Circulation Models (OGCMs) the problem is more challenging because the lateral boundary conditions are not known [*Pedlosky*, 1996], and in OGCMs used for climate studies quasi-geostrophic turbulence is generally not resolved. The combination of numerical and physical constraints makes it difficult to arrive at a formulation of viscosity that is universally applicable or accepted [see, e.g., *Griffies and Hallberg*, 2000; *Large et al.*, 2001; *Lengaigne et al.*, 2003; *Pezzi and Richards*, 2003].

[4] The fundamental challenge in chosing the optimal viscosity is that it should be large enough to suppress numerical instabilities on the grid scale (hereafter simply noise) but small enough to allow the model to reproduce sharp fronts and mesoscale activity where the resolution permits it. A particular concern is to obtain a realistic structure of topographically controlled flow because it controls much of the sea ice distribution (see sections 6–8). However, it is also true (at least for the present study) that most gridscale noise is generated by flow over steep topography. Thus the desire for uniformly low grid scale noise demands large viscosity, although one might prefer to minimize viscosity to optimize the ocean simulation. In principle this problem could be avoided by simply increasing the resolution of OGCMs. However, for the foreseeable future the required resolution makes this too expensive for climate applications. Given the computational constraints it is then natural to ask how much the solution can be improved by reducing viscosity, and how much more grid scale noise one has to accept in return.

[5] It is shown here that reducing viscosity in the ocean component of a fully coupled climate model (or General Circulation Model, GCM) does indeed lead to an improved solution at the price of larger levels of noise (although the particular compromise may not be optimal yet). The study focuses on five subregions of the global ocean, in particular

---

[1]Oceanography Section, National Center for Atmospheric Research, Boulder, Colorado, USA.

it explores how in each of these viscosity affects the local dynamics and (indirectly) thermodynamics. The respective sections are rather different in scope and depth, reflecting different states of knowledge and data coverage. For example, the equatorial Pacific is well studied and observed, making it straightforward to connect the present results with the framework of equatorial oceanography. On the other hand, the results for the Antarctic Circumpolar Current (ACC) indicate an important role for lateral viscosity, something which has not received much attention in the literature. Thus we look at the equatorial results as just one more piece in an already complex puzzle, whereas the ACC results present a starting point from which one can take a fresh look at Southern Hemisphere dynamics. Also, because of different data coverage quantifying the improvements is relatively simple in the equatorial Pacific but rather difficult in the Arctic ocean.

[6] The next two sections discuss the experimental setup and global features of the solution. The following sections then discuss the regional impacts of low viscosity on five different regimes: the eddy permitting equatorial Pacific (section 4), the topographically controlled ACC (section 5), the sea-ice covered Arctic ocean (section 6), the western boundary current of the North Pacific (section 7) and the boundary currents around Greenland (section 8). A discussion concludes this study.

2. Description of Model and Experiments

[7] The numerical experiments are performed using the National Center for Atmospheric Research (NCAR) Community Climate System Model version 3 (CCSM3) which consists of the fully coupled atmosphere, ocean, land and sea ice models; a detailed description is given by *Collins et al.* [2006].

[8] We use the T42x1 resolution version of the model in its present-day setup. The ocean model (Parallel Ocean Program, POP) has a horizontal resolution that is constant at $1.125°$ in longitude and varies from $0.27°$ at the equator to approximately $0.7°$ in high latitudes. In the vertical there are 40 depth levels; the uppermost layer has a thickness of 10 m, the deepest layer has a thickness of 250 m. The atmospheric model (Community Atmosphere Model, CAM3) uses T42 spectral truncation in the horizontal (about $2.8°$ resolution) with 26 vertical levels. The sea ice model shares the same horizontal grid as the ocean model and the land model is on the same horizontal grid as CAM3. Details of the coupling are described by *Danabasoglu et al.* [2006]. The tracer advection scheme of POP is the third-order upwind scheme [*Holland et al.*, 1998], which presents a compromise to minimize dispersion as well as diffusion. To avoid singularities in the Arctic Ocean POP uses a displaced pole grid: The grid south pole is identical with the geographical South Pole and in the Southern Hemisphere the grid is a regular latitude/longitude grid, but the grid north pole is located over Greenland. Thus in the northern hemisphere the grid-x and grid-y directions are generally not eastward or northward.

[9] For the present study the most relevant aspect of the model formulation is the horizontal viscosity parameterization of the ocean model. Here, the momentum equations use the *Large et al.* [2001] anisotropic horizontal viscosity, as

Table 1. Settings Used for the Viscosity Parameters Defined in the Appendix for CONT, NOSMAG, and LOWVISC

Parameters	CONT	NOSMAG	LOWVISC
A_{SGS}: A_{eddy}, m² s⁻¹	1000	1000	600
B_{SGS}: B_{eddy}, m² s⁻¹	1000	1000	300
C_2	0	0	$\frac{1}{2}\left(\frac{A_{eddy}}{B_{eddy}}-1\right)$
ϕ_I, ° latitude			30
A_{SMAG}: C_A	8	0	0
B_{SMAG}: C_{eq}	0.16	0	0
C_{lim}	8	0	0
A_{NOISE}	A_{GRe}	A_{GRe}	B_{MUNK}
B_{NOISE}	B_{MUNK}	B_{MUNK}	B_{MUNK}
A_{VCFL}	$\dfrac{(\Delta x^{-2}+\Delta y^{-2})^{-1}}{2Dt}$	$\dfrac{(\Delta x^{-2}+\Delta y^{-2})^{-1}}{2Dt}$	$\dfrac{(\Delta x^{-2}+\Delta y^{-2})^{-1}}{2Dt}$
f_V	$\frac{1}{2}$	$\frac{1}{2}$	$\frac{1}{2}$
ALIGN	E-W	E-W	E-W

generalized by *Smith and McWilliams* [2003]. In addition to background values, the viscosity depends on the local deformation rate of the flow as by *Smagorinsky* [1993], on the distance from the western boundary to resolve the frictional boundary layer [*Munk*, 1950], and on minimum (Reynolds number criterion, RC) and maximum (viscous Courant-Friedrichs-Levy Criterion, VCFL) constraints to ensure numerical stability. Since numerical stability depends, among other things, on grid size and velocity, lateral viscosity is chosen to be anisotropic as given by two viscosity coefficients A and B, which can vary in space and time. It should be noted that while the three considerations above provide reasonable guidelines for choosing ocean viscosity, they were not derived with OGCMs in mind: *Smagorinsky* [1963] has been developed as a parameterization for isotropic 3d-turbulence [see also *Fox-Kemper and Menemenlis*, 2007], and the Munk layer is a concept that arose in discussing the dynamics of shallow-water ocean models [*Pedlosky*, 1996]. Similarly, satisfying RC will ensure the suppression of gridscale noise, but as pointed out by *Weaver and Sarachik* [1990] the RC is only a necessary but not a sufficient condition for instability. For example, *Large et al.* [2001] illustrated that it may be sufficient to satisfy this criterium in only one horizontal dimension. The details of the horizontal viscosity formulation and the related parameter values are given in Appendix A and Table 1, respectively.

[10] The simulation with the horizontal viscosity above represents our control case (denoted as CONT). In NOSMAG, we eliminate the dependency of A and B on the local deformation rate, i.e., no Smagorinsky based parameterization is used (see Table 1). Otherwise, this case is identical to CONT. In LOWVISC viscosity is reduced further: the background value of the subgrid scale (SGS) viscosity A_{SGS} is reduced globally from 1000 to 600 m² s⁻¹; and the value of B_{SGS} is lowered from 1000 to 300 m² s⁻¹ between 20°S and 20°N, increasing meridionally to a value of 600 m² s⁻¹ poleward of 30° latitude and staying constant thereafter. In addition, we no longer impose RC as a numerical constraint on A. Instead, to diminish numerical noise propagating from the western boundaries to the ocean interior, the *Munk*-based criterion

is applied not only for B but also for A. This significant reduction of viscosity in LOWVISC has originally been motivated by our desire to reproduce tropical instability waves (TIWs), a major component of the equatorial ocean heat budget. *Jochum et al.* [2004] showed that with resolution and viscosity similar to the ones chosen in LOWVISC, TIWs can be reproduced realistically.

[11] In all cases, the ocean model is initialized with the January-mean climatological potential temperature and salinity (a blending of *Levitus et al.* [1998] and *Steele et al.* [2001] data sets) and zero velocities. The remaining components are initialized with January conditions obtained from stand-alone integrations. The numerical experiments are integrated for 120 years. The present analysis is based on the means of years 101–120. Most of the presented results are based on a comparison between LOWVISC and CONT, an exception is the discussion on the Labrador Sea where the change from NOSMAG to LOWVISC does not change the solution appreciably.

[12] The time-mean distributions of the anisotropic horizontal viscosity coefficients A and B at 100-m depth are shown in Figure 1. The Smagorinsky component of viscosity is identical in both A and B polewards of about 40° latitude (Figures 1a and 1b; Appendix A). This part produces viscosities of $\mathcal{O}(10000)$ m^2 s^{-1}, not only along western boundary currents but also in areas of barotropic flow over steep topography (like the Southern ocean or the subpolar gyres).

[13] Although our choice for the tunable Smagorinsky scaling coefficient is within the common range [*Griffies*, 2004], the resulting viscosities are clearly much larger than the estimates based on observed float dispersion [e.g., *Freeland et al.*, 1975]. A and B from CONT are dominated by these large viscosities between about 30°–75° latitude, particularly evident in Figure 1b for B. Near the western boundaries, B gets larger due to the Munk criterion (Figure 1b). At both low latitudes and polewards of 75° latitude, the grid Reynolds number dependent part of the viscosity formulation, i.e., A_{GRE} (see Appendix A) becomes important in A (Figure 1a). However, these A_{GRE}-based values exceed what is allowed based on the viscous CFL criterion, i.e., A_{VCFL} (see Table 1), between 10°S and 10°N. Consequently, A_{VCFL} is applied in this latitude band.

[14] In NOSMAG both A and B are much reduced between 30°–75° latitude (Figures 1c and 1d). For example, along the latitude band of the Southern Ocean, A and B are $\mathcal{O}(5000)$ and 600 m^2 s^{-1}, respectively, compared to $\mathcal{O}(10000)$ m^2 s^{-1} or larger in CONT. In LOWVISC, the largest viscosities are confined to the western boundary regions in both A and B (Figures 1e and 1f). Elsewhere, A has a globally uniform value of 600 m^2 s^{-1} while B varies from 300 m^2 s^{-1} near the equator to 600 m^2 s^{-1} polewards of 30° latitude. This is consistent with recent studies by *Theiss* [2004] and *Eden* [2007] who provide evidence from high resolution models that eddy mixing lengths are isotropic poleward of approximately 30° latitude, and anisotropic (with zonal mixing lengths exceeding meridional lengths) equatorward of this.

[15] One drawback of reduced viscosity is increased gridscale noise. Most of this noise is found in the variation of velocity in grid-y direction (v) along the grid-x direction (in the southern hemisphere this is equivalent to zonal variation of meridional velocity, but because of the displaced northern pole of the ocean grid, it is different in the northern hemisphere). Thus for the present purposes noise is defined as:

$$dxn = |v - vs|,$$

where vs is v smoothed in the grid-x direction with a three point triangular filter (weights: 0.25, 0.5, 0.25). We experimented with different definitions of noise, but all gave similar results. Compared to CONT, the level of noise in NOSMAG and LOWVISC is slightly increased in the tropics and has more than doubled (Figure 2) in high latitudes.

[16] The noise in the tropics and subtropics is created by the western boundary currents, a result consistent with *Griffies et al.* [2000]. The reason for the relatively small values there, and the small differences between the experiments, is that in all experiments the viscosity along the western boundary is set to resolve the Munk layer; thus, the noise is small by design. Further inspection of the model fields shows that increased noise at higher latitudes can result from the interaction between barotropic flow and bottom topography. The weakly stratified flow of high latitudes simply follows the bottom topography, and grid scale noise in the flow can be generated by gridscale variations in topography. Wave number spectra are one possible way to quantify the extent to which noise is topographically or numerically induced.

[17] The spectra are based on the mean kinetic energy (KE) at 900 m depth (Figure 3) and on mean Sea Surface Height (SSH) along 58°S, a band that is not obstructed by land. For both variables the spectra for LOWVISC and NOSMAG are almost identical, whereas CONT shows reduced energy for wavelengths smaller than 1500 km for KE, and reduced energy for wavelengths smaller than 600 km for SSH. For longer wavelengths it is not clear which of the spectra is the most realistic, but it is obvious that for KE none of the experiments suffers from increased energy at the gridscale, whereas for SSH all of them do. This is also true for the other unobstructed depths or latitude bands. The level of SSH energy on the gridscale (noise) is larger in LOWVISC than in CONT, but so is the energy on larger scales (signal).

[18] The reason that gridscale noise exists in SSH but not in KE is that the barotropic and baroclinic modes are solved for differently [*Dukowicz and Smith*, 1994], and the barotropic mode has a 'checkerboard null-space' which makes it susceptible to gridscale noise [*Killworth et al.*, 1991]. However, the only way the checkerboard SSH field can change the dynamics is through the vertical velocity and the continuity equation. Experience so far has shown that this leads to no serious problems with the model simulations [*Smith and Gent*, 2002], and indeed, the spectra of the

Figure 1. Anisotropic horizontal viscosity coefficients A and B at 100-m depth from (a–b) CONT, (c–d) NOSMAG, and (e–f) LOWVISC. Units are 1000 m^2 s^{-1}. All panels use the same color scale.
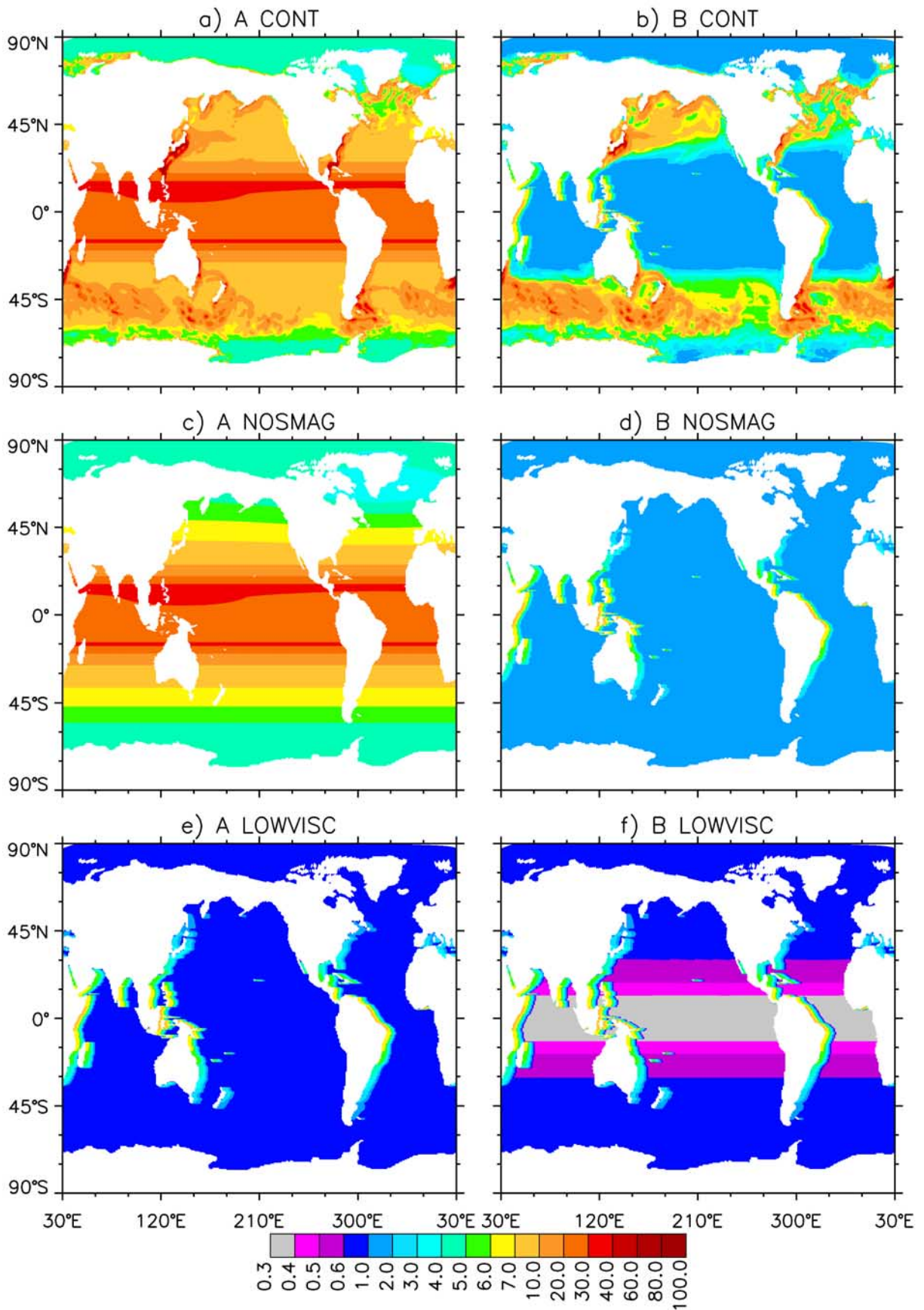
Figure 1
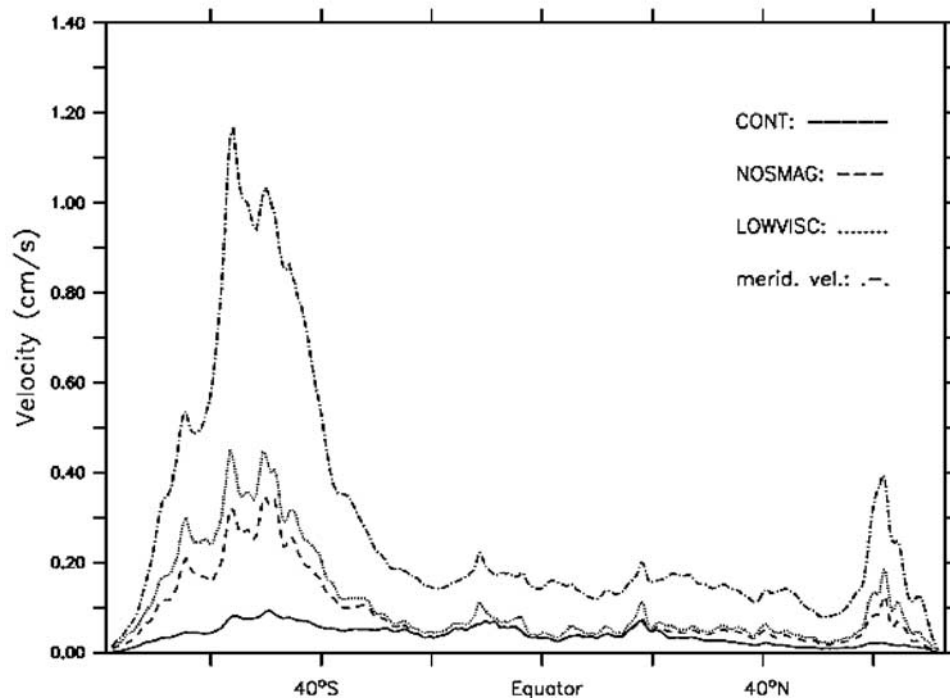
Figure 2. Zonally averaged gridscale noise for CONT, NOSMAG, and LOWVISC. For comparison the mass averaged absolute velocity in grid-*y* direction for LOWVISC is shown as well.

vertical velocity, like the KE spectra, do not show increased energy at the smallest scales (not shown).

[19] We conclude that compared to CONT, the noise level in NOSMAG and LOWVISC are increased, but nowhere to a level where it affects adversely the performance of CCSM3 as a climate model. However, the present study does not rule out the possibility that for certain applications it may be benefitial to add a Smagorinsky component to the viscosity. To understand the sensitivity of CCSM3 to the value of the Smagorinsky component, a short (20 year) integration of CCSM3 (branched of CONT at year 100) has been performed in which the Smagorinsky component is reduced to one eighth of the CONT values. The means of the last 10 years show that current transports, SST changes, and noise values fall in between the values for CONT and NOSMAG. In this run the Smagorinsky component of viscosity only rises above the background and Munk values where the ACC flows over steep topography and around the coasts of Greenland, Iceland and Norway (not shown). This suggests that in an OGCM Smagorinsky viscosity effectively works as a parameterization for the interaction between flow and topography. It has not been designed for that purpose, but without further research one cannot rule out the possibility that there is indeed enhanced dissipation of momentum over, for example, the topographic ridges of the Southern Ocean.

3. Global Results

[20] Gridscale noise is unwanted because it can potentially increase tracer gradients and thereby lead to spurious diffusion. The change in globally averaged mean stratification is one possible metric by which to judge spurious diffusion. In NOSMAG and LOWVISC the stratification is almost identical to the one in CONT (not shown). The maximum stratification in the thermocline is reduced by approximately 1%, which is small compared to the already existing weak bias of 10% compared to *Levitus et al.* [1998].

[21] It is plausible [*Griffies et al.*, 2000], that this weakening of the thermocline is caused by increased diapycnal diffusion; therefore the increase in noise will have to be justified by an improved overall solution.

[22] To put the present results into perspective we will, where relevant and possible, compare them with the results of *Roberts et al.* [2004, HAD from here on] and *Griffies et al.* [2005, MOM from here on]. Both studies discuss GCM experiments that are similar to CCSM3 in complexity and resolution. In HAD the experiment consisted of increasing the horizontal resolution in the ocean from uniformly $1.25° × 1.25°$ to $1/3° × 1/3°$, accompanied by a reduction of viscosity. In MOM the experiment consists of reducing the ocean viscosity poleward of 20° latitude. We think of our model setup as a companion case: the resolution is kept constant, but the viscosity is reduced everywhere. The results presented below indicate, however, that the effects of our modifications are closer to HAD than MOM. It is beyond the scope of the present study to understand the differences in the results of HAD, MOM, and LOWVISC. Rather, we will note the differences for the orientation of the reader and focus on the dynamical processes in selected subregions.

[23] An important aspect of the coupled solution is the strength of the meridional overturning circulation (MOC) and the associated poleward heat transport. Reducing viscosity changes the maximum strength of both by less than
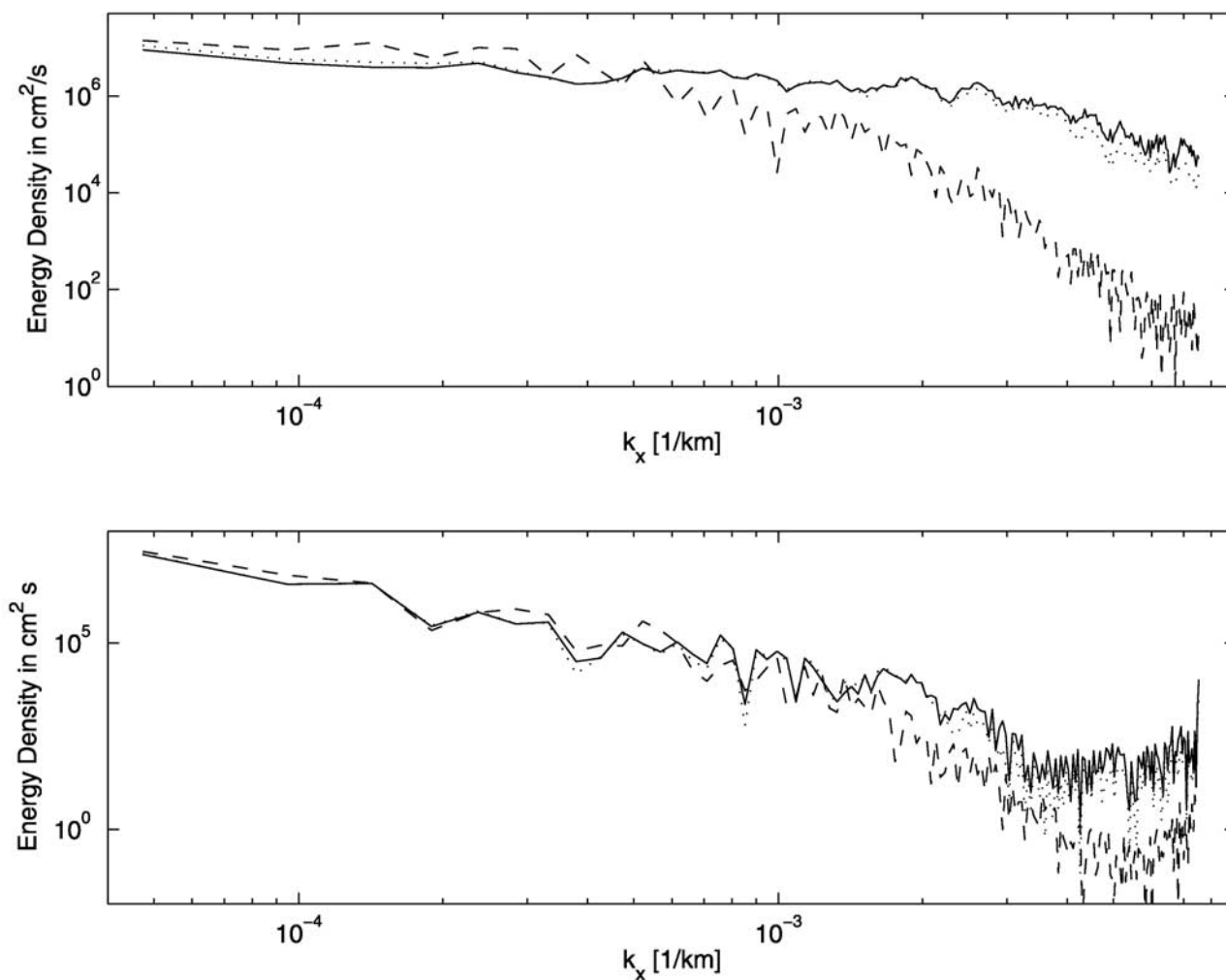
Figure 3. Zonal spectrum of mean kinetic energy at 900 m depth (top) and SSH (bottom) along 58°S for CONT (dashed), NOSMAG (dotted) and LOWVISC (solid).

5%: the deep MOC maximum in the Northern Hemisphere is between 20 and 21 Sv in all cases, and the maximum northward heat transport in the Atlantic is between 1.00 and 1.05 PW. This is consistent with HAD, but very different from MOM which shows a substantial increase in the MOC associated with Labrador Sea convection. In all simulations the net ocean heat uptake is negligible: a net warming of less than 0.20 W/m². The zonally integrated mean wind stress, too, is almost identical. However, locally there are differences, and they will be discussed in the following sections.

[24] With the exception of the ACC the main transports, too, are largely unchanged. In all cases the Florida Strait transport is between 28 Sv (CONT) and 32 Sv (LOWVISC), and the Indonesian Throughflow transport is 17 Sv. A surprising result is that the ACC transport through the Drake passage is reduced from 171 Sv in CONT to more realistic 150 and 142 Sv in NOSMAG and LOWVISC, respectively. Thus smaller viscosity results in smaller transport; this will be discussed in detail in section 5. These changes in the ACC transport are consistent with HAD, but of opposite sign than those in MOM.

[25] Inspection of the model fields shows that the largest changes to the solution are in annual mean Sea Surface Temperature (SST, Figure 4) and sea ice (Figure 5). RPH The large changes in SST and sea ice poleward of 50°N are of opposite sign than the biases, and generally present improvements to CONT. Mostly they are realized already in NOSMAG and their surprising magnitude is largely the result of the positive sea-ice - albedo feedback (sections 6 and 8). The changes in the western boundary currents reduce the biases in the Kuroshio (section 7), increase the biases in the Gulf Stream, and on average leave the SST biases unchanged in the Agulhas retroflection region. The changes along the ACC are due to a narrowing of its core and the resulting changes in the isothermal slopes (section 6; for a detailed discussion of the SST biases in CONT see *Large and Danabasoglu* [2006]). Along the equatorial Pacific reducing viscosity from NOSMAG to LOWVISC leads to warming of the equatorial cold tongue which reduces the bias there (see also section 4). However, in spite of the improvements in equatorial SST the simulation of ENSO did not improve. In all cases, the peak in ENSO variance is at periods between 1.5 and 2.5 years, and in all runs there is too little energy at low frequencies (see *Deser et al.* [2006] for a discussion of ENSO in CCSM3). The standard deviations of interannual NINO3 (5°S–5°N, 150°W–90°W) SST variability are 0.77 for CONT, 0.80 for
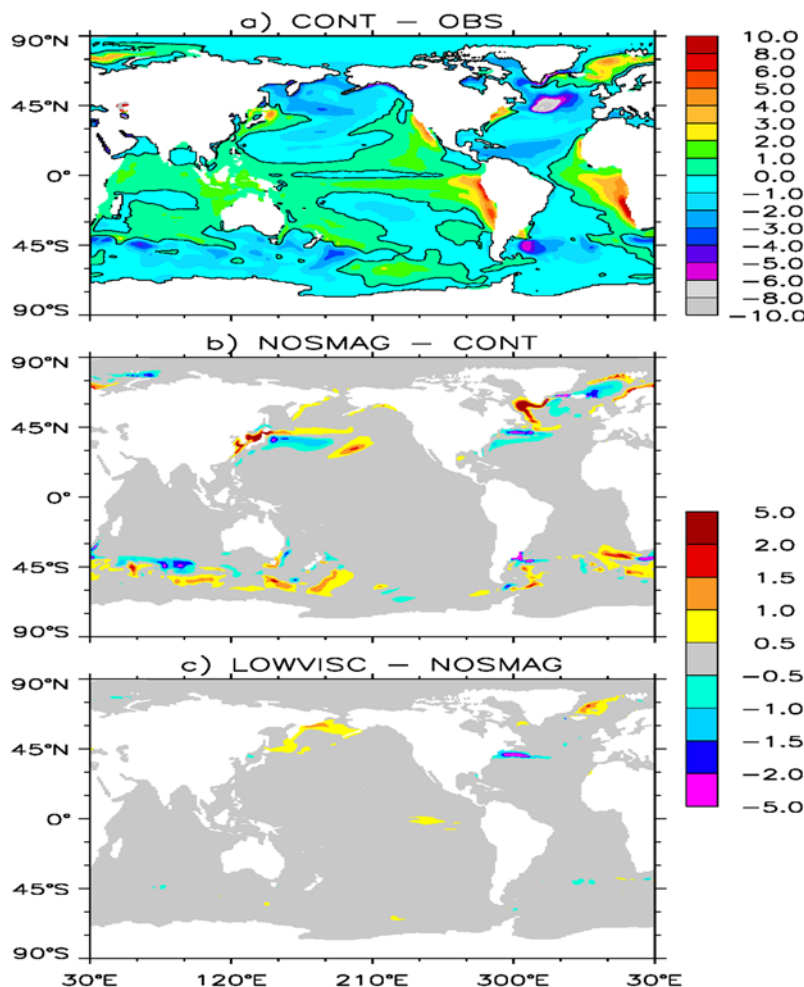
Figure 4. Difference in SST between CONT and *Levitus et al.* [1998] (a), between NOSMAG and CONT (b) and between LOWVISC and NOSMAG (c).

NOSMAG and 0.63 for LOWVISC. One can speculate that the significantly lower amplitude in LOWVISC is due to the warmer equatorial cold tongue, which reduces the zonal SST gradient and therefore the size of the ENSO induced anomalies. However, ENSO is rather unrealistic in all three experiments, so that the reason for this weakening will not be investigated further. It is worthwhile to point out that recent work by *Neale et al.* [2008] demonstrates that the shortcomings in the CCSM3 ENSO are solely due to missing physics in the CAM3 convection scheme.

[26] In general, the changes in precipitation, winds, and sea level pressure induced by a change in ocean viscosity are small, especially if compared with current biases. The exceptions are locally confined and tied to the changes in the western boundary currents like the Kuroshio, Gulf Stream, and Agulhas Retroflection. The changes in the midlatitude North Pacific will be discussed in section 7 as an example for western boundary regimes. This general finding that an improved representation of the ocean leads to only minor improvements in the overlying atmosphere is consistent with HAD.

[27] The analysis presented so far shows that the drawbacks of reducing ocean viscosity are rather minor. The following sections illustrate that there are key aspects of the ocean model solution where reducing viscosity leads to major improvements: equatorial Pacific (section 4), ACC (section 5), Arctic Ocean (section 6), Kuroshio (section 7) and Labrador Sea (section 8).

4. Equatorial Pacific

[28] Improving the ocean circulation in the equatorial Pacific has been the original motivation for reducing the viscosity. The hypothesis is that reducing viscosity allows for tropical instability waves (TIW) [*Cox*, 1980], which would then, because of their strong meridional heat flux [*Hansen and Paul*, 1984], remove the cold bias in the central and eastern equatorial Pacific. This should also improve the seasonal cycle of SST and precipitation there, and lead to an improved simulation of ENSO. As it turns out, neither the seasonal cycle nor ENSO improved notably and the real improvements to climate are found in higher latitudes. However, TIWs are stronger in LOWVISC and the mean state of the equatorial Pacific is improved, both of which is documented in this section.

[29] TIWs are created by shear instabilities of the zonal equatorial currents and have periods between 20 and 40 days and wavelengths between 500 and 1500 km

[e.g., *Legeckis*, 1977]. Their dynamics lead to strong horizontal [*Hansen and Paul*, 1984] and vertical [*Jochum and Murtugudde*, 2006] mixing. The 20 year current

meter record from the TAO observing system suggests that on the equator at 140°W TIWs have a mean eddy kinetic energy (EKE) of approximately 500 cm^2 s^{-2} with extrema between 200 and 700 cm^2 s^{-2}, stronger during La Niña, weaker during El Niño. In CONT and NOSMAG their EKE is only 60 cm^2 s^{-2}, whereas in LOWVISC it is increased to 360 cm^2 s^{-2}.

[30] To understand the importance of TIWs for the mixed layer heat budget, one can quantify the meridional advection of temperature $((vT)_y)$ due to resolved eddies and parameterized subgrid scale processes (diffusion). Even with weak or absent TIWs in CONT and NOSMAG explicit and implicit numerical diffusion causes a substantial equatorward temperature advection (not shown). In the upper 30 m between 140°W and 110°W the equatorward temperature advection in CONT is approximately 1.0°C month^{-1}; better representing TIWs as in LOWVISC, increases the maximum temperature advection to 1.5°C month^{-1}. This is consistent with results from an Atlantic OGCM study by *Jochum et al.* [2005], which shows that on the equator under identical forcing resolving TIWs increases the resolved and unresolved eddy temperature advection by 30%. At the equator there are several observational estimates available (for the mixed layer); at 140°W their estimations range between 0.8 and 1.3°C month^{-1}, and at 110°W the range is between 1.3 and 2.6°C month^{-1}, with observational uncertainties of up to half of the estimated means [*Hansen and Paul*, 1984; *Bryden and Brady*, 1989; *Baturin and Niiler*, 1997; *Jochum et al.*, 2007]. The LOWVISC values at these points are 1.2 and 2.0°C month^{-1}, respectively. Thus the values for EKE and for the meridional temperature advection both suggest that at least near the surface the TIWs in LOWVISC are reasonably well represented.

[31] The increased meridional temperature advection leads to an improved equatorial SST, most notably the cold bias of the equatorial cold tongue in the central Pacific has been reduced (Figure 6, bottom). However, this improvement in the mean SST does not lead to any significant improvements in equatorial winds or precipitation (not shown). The fact that including TIWs leads to an improved SST in the equatorial cold tongue, but not significant changes in tropical climate is consistent with HAD, who suggest that in coupled GCMs there is no need to increase horizontal resolution in OGCMs beyond 1/3° until the corresponding AGCMs feature a resolution high enough to respond to the resolved oceanic features.

[32] Last, we will discuss the changes to the equatorial current structure. The Pacific Equatorial Undercurrent (EUC) is probably ideally suited to study viscosity because it is well observed and the dynamics are not complicated by topography. However, since *Harrison* [1978] it became clear that there is no robust correlation between mean gradients and eddy-fluxes. Thus choosing the optimal viscosities is still very much a matter of trial
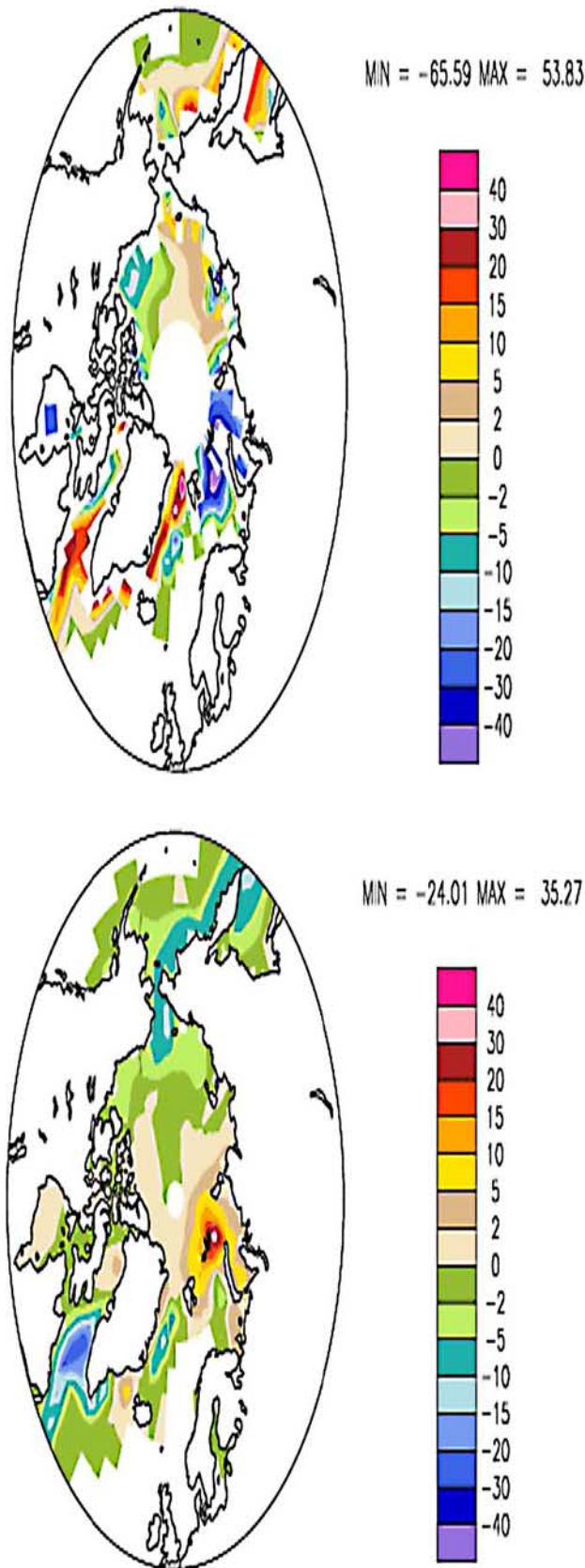
Figure 5. Difference in annual mean sea ice concentration between CONT and observations [*Rayner et al.*, 2003, top] and between LOWVISC and CONT (bottom). Colorbar denotes the difference in percentage of the surface of an ocean grid cell that is covered by sea ice.
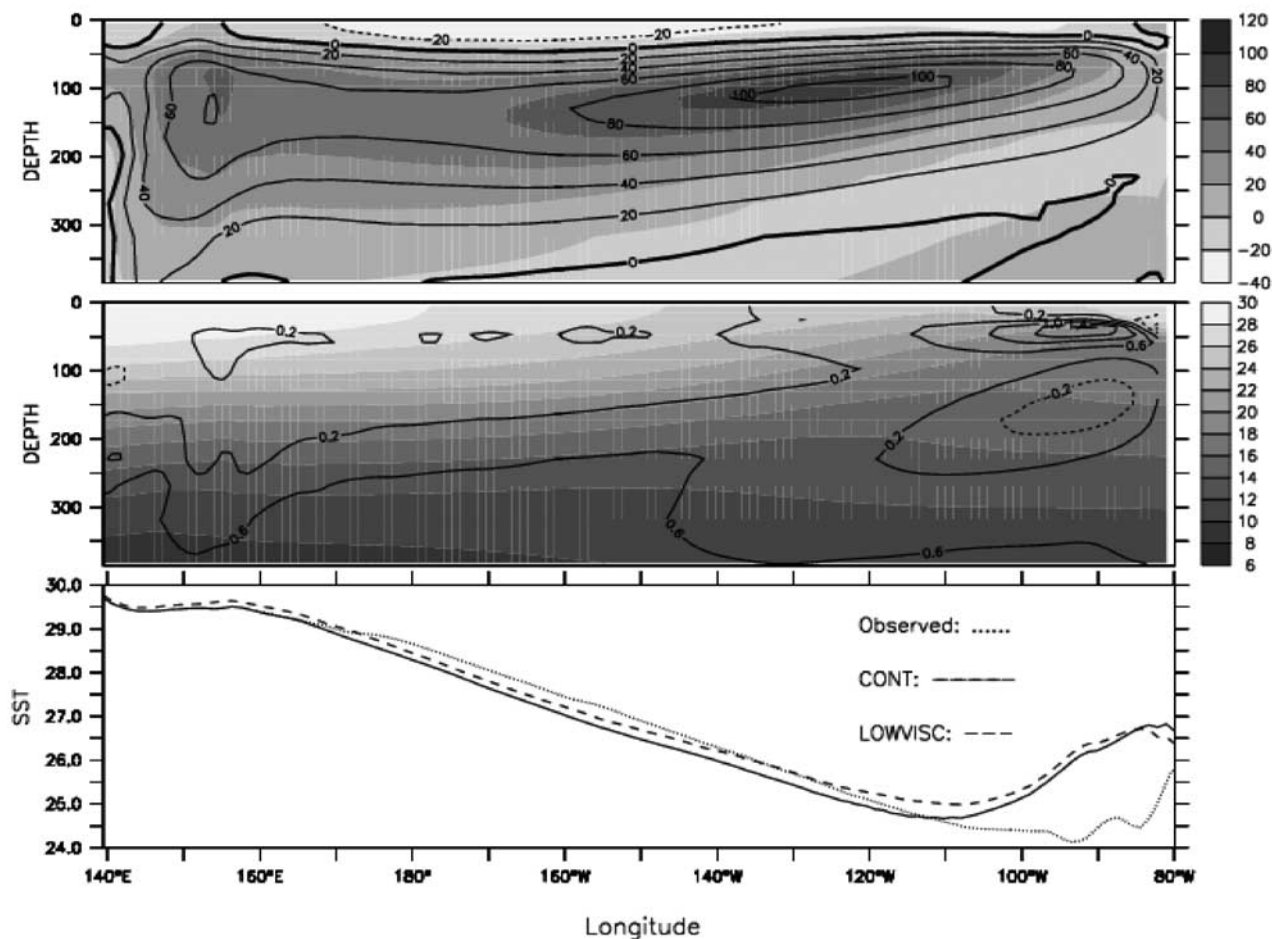
Figure 6. Top: Zonal velocity along the equator in CONT (gray shades) and LOWVISC (contour lines: 20 cm s^{-1}). Center: Temperature along the equator in CONT (gray shades) and its increase in LOWVISC (contour lines: 0.4°C). Bottom: SST between Papua New Guinea and Ecuador, averaged between 2°S and 2°N (observations based on *Reynolds and Smith* [1994]). The maximum warming between LOWVISC and CONT is at 110°W with 0.5°C.

and error. The studies by *Maes et al.* [1997] and *Pezzi and Richards* [2003] both conclude that in OGCMs a value of horizontal viscosity of approximately 1000 m^2 s^{-1} gives reasonable results for the strength and structure of the EUC. Lower viscosities lead to a stronger EUC with a deeper core. In particular the deeper core is unrealistic, and it has been demonstrated by *Maes et al.* [1997] that this is because vertical diffusion of momentum increases as the horizontal viscosity is reduced. This is consistent with the present results; here, however, we argue that viewed as a whole the equatorial circulation becomes more realistic. In LOWVISC the core indeed becomes deeper (Figure 6, top), especially in the far east (at 110°W it dropped from 70 m in CONT to 90 m in LOWVISC, compared to 75 m in the observations), but the model now has a more realistic maximum velocity of the EUC. The deepening of the core in the east leads to increased stratification there, because cool thermocline water reaches the surface further east, thus increasing the stratification in the east (Figure 6, center). At the longitude of the maximum velocity (125°W), the observed maximum EUC speed is 113 cm s^{-1}, in CONT it is 92 cm s^{-1} and in LOWVISC it is 105 cm s^{-1}. The

representation of Subsurface Countercurrents [SSCCs, *Tsuchiya*, 1975] is also improved. The observations show them as subsurface maxima in eastward velocity at 5°S and 4.5°N, with maximum speeds of 10 and 14 cm s^{-1}, respectively (Figure 7). In CONT their cores are rather diffuse, whereas in LOWVISC their cores are separated from the EUC, and have a stronger, more realistic maximum velocity. The improved Tsuchiya Jets are a desirable feature since they supply the water for the upwelling in the Costa Rica dome and off the coast of Peru [*McCreary et al.*, 2002]. Obviously, the equatorial current structure still has biases and the most glaring one is the poor representation of the NECC (eastward core at 6°N). Its weakness is partly a reflection of deficiencies in the simulation of tropical winds, but also due to the coarse atmospheric resolution which, even if the winds were perfect, cannot create the strong windstress curls that force the NECC.

[33] The fact that reducing viscosity below the more commonly used values of around 1000 m^2 s^{-1} leads to a general improvement in the equatorial circulation, but comes at the price of an unwanted deepening of the EUC core is a problem. For a coupled GCM, where a
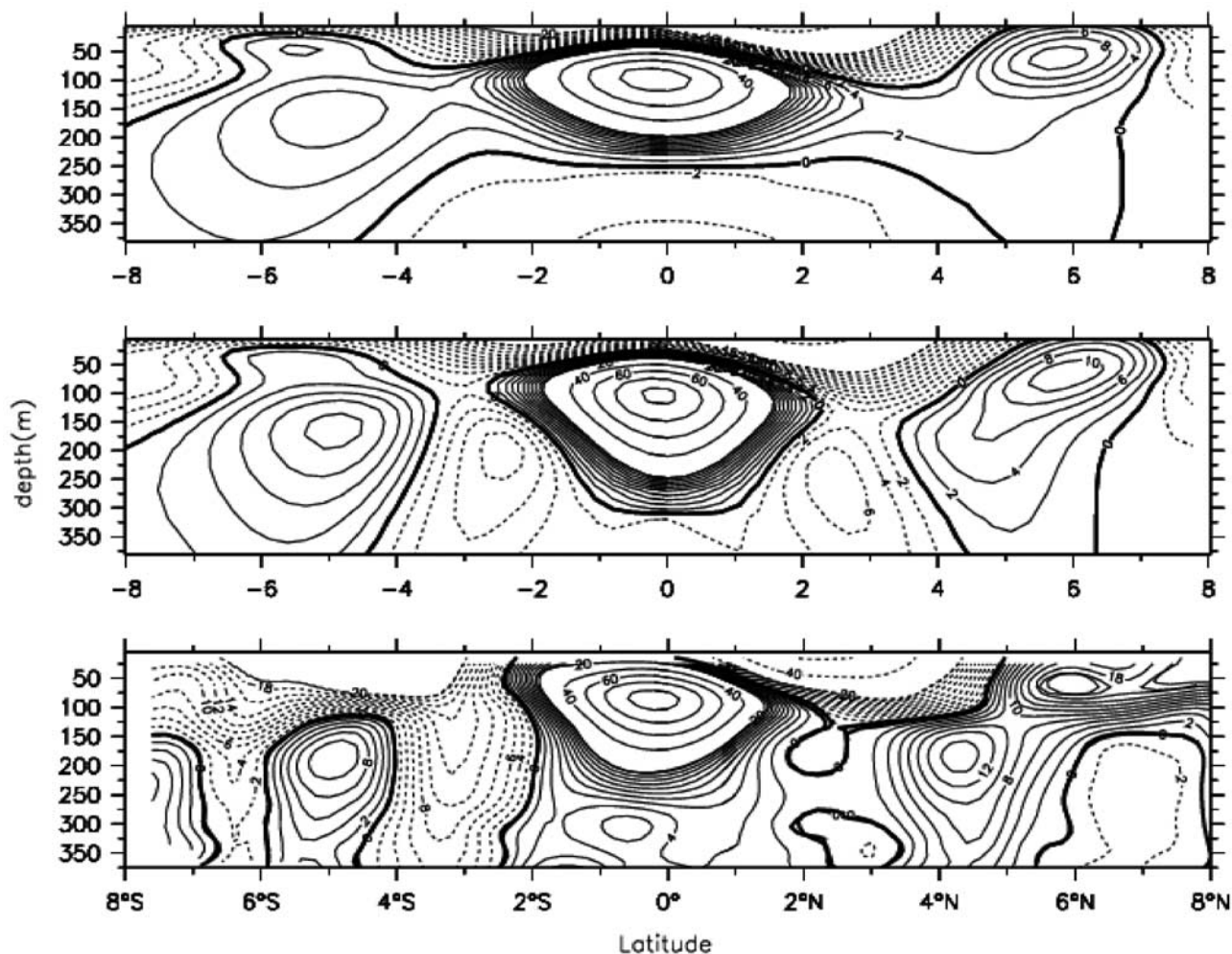
Figure 7. Zonal velocity across 125°W in CONT (top), LOWVISC (center) and observations (bottom, from *Johnson et al.* [2001]). The contour interval is 20 cm s^{-1} and 2 cm s^{-1} for velocities with an absolute value smaller than 20 cm s^{-1}; eastward velocities are contoured solid, westward velocities dashed.

realistic SST is of considerable importance, reducing viscosity is an attractive choice. However, one is still left with a fundamental problem: what happens to the momentum of the EUC in the eastern basin? Reducing vertical viscosity below the core has been tried by the present authors and does lift the core marginally, but obviously this does not remove the excess momentum. One possibility is that in the model TIWs do not remove sufficient momentum, and indeed, the TIWs are too confined to the surface (not shown). The study by *Maes et al.* [1997] points to another interesting possibility: the transfer of mean kinetic energy to TIWs is exceeded by a factor of 3 by the transfer to mean potential energy. Thus this would call for increased thickness diffusion to slow down the EUC, something that has indeed been found by *Danabasoglu and Marshall* [2007] but still needs more research and understanding.

5. The Antarctic Circumpolar Current

[34] As discussed in section 3, the ACC transport decreases as the viscosity is reduced. However, the mean kinetic energy of the ocean south of 40°S is about 30%

larger in LOWVISC than in CONT, and the energy input into the ACC by the winds is almost identical in all three experiments (not shown).

[35] The time-mean speed across Drake Passage (DP) shows a diffuse current with a maximum speed of about 30 cm s^{-1} in CONT (Figure 8b). In contrast, the current is much tighter with velocities exceeding 60 cm s^{-1} in LOW-VISC (Figure 8a). When the ACC transports are computed across this passage, the weaker but wider current in CONT happens to produce a larger ACC transport compared to the stronger but narrower current in LOWVISC. The transport in LOWVISC (142 Sv) is closer to the observational estimates of 137 ± 8 Sv [*Whitworth and Peterson*, 1985; *Cunningham et al.*, 2003] than the transport in CONT (171 Sv), but the observations of the transport as well as the oceanic forcing fields are rather uncertain, so that the ACC transport alone cannot be used to constrain horizontal viscosity. However, the vastly different widths of the currents (Figure 8) suggests that, at least near DP, velocity shear data (once available in good temporal coverage) can be used to constrain viscosity in OGCMs. For example, the 6 hydrographic sections by *Cunningham et al.* [2003] show that the ACC transport
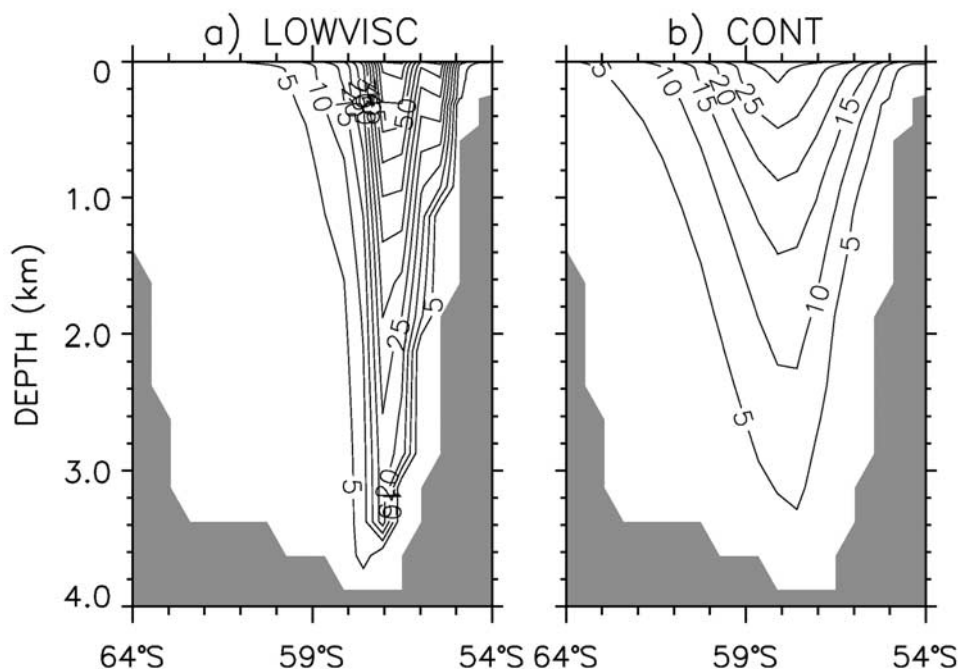
Figure 8. Time-mean speed across the Drake Passage at 65°W. The contour interval is 5 cm s^{-1}.

across 56°W is carried by 2 separate jets which are present in LOWVISC but not in CONT (not shown).

[36] Traditional ACC studies (see *Olbers et al.* [2006] for a recent review) focus on the ACC transport and assume that the impact of eddy momentum transport on the ACC is secondary to other effects. Obviously this is not the case here. Also important for the DP transport are the smaller viscosities along the Antarctic coast in LOWVISC and NOSMAG, which allow stronger westward flow in response to the westward wind stress along the continent (not shown). This also acts to reduce eastward transport in these cases. It is interesting to note that a recent numerical study by *Hallberg and Gnanadesikan* [2006] found that the DP transport decreases with increased resolution (and reduced viscosity). This result is consistent with the present result, but the explanation is not: Whereas they attribute the reduction in transport to the strengthening of the mesoscale eddies, none of the present experiments have significant eddy kinetic energy in the Southern Hemisphere.

[37] Although thickness diffusivity, which is the primary ocean parameter that controls the isopycnal slopes [*Danabasoglu and McWilliams*, 1995], is constant across the cases, there are some modest changes in these slopes. This is due to the reduced transport in LOWVISC, and consequently smaller zonal velocities, which directly affects the density field through geostrophy. In particular, the density in LOWVISC is lower to the south of the ACC in the upper 1000 m (not shown) which accounts for the warmer SST there (Figure 4).

[38] *Gent et al.* [2001] suggest that the DP transport is largely set by the southward transport in the intermediate layer of the ocean at the latitude band of the DP. This intermediate layer occupies the vertical region below the surface Ekman layer and above the minimum depth of the topography. The present results are consistent with *Gent et al.* [2001], because the southward transport at the latitude

band of the DP is indeed lower in the intermediate layer in LOWVISC and NOSMAG (not shown). However, the present study does not provide evidence that the southward transport forces the zonal transport, it shows merely that the two are correlated.

6. The Arctic Ocean

[39] Observations [e.g., *Dickson et al.*, 2007] and high resolution model simulations [*Maslowski et al.*, 2004] show that Atlantic inflow enters the Arctic through two pathways: via the Barents Sea Inflow (BSI, between Spitsbergen and Siberia) and via the West Spitsbergen Current (WSC). Observed estimates (Table 2) of transports within these inflow branches vary widely [e.g., see *Carmack*, 1990; *Rudels and Friedrich*, 2000] with more recent estimates suggesting a roughly equal volume transport between the two [e.g., *Rudels and Friedrich*, 2000; *Karcher et al.*, 2003; *Maslowski et al.*, 2004].

[40] In CONT, the WSC is too weak (0.3 Sv) and the BSI too strong (4.7 Sv). In response to lower viscosity, the strength of the former increases to 1.1 Sv, leading to an increase in heat transport from 8 to 26 Terawatts (TW, 10^{12} Watts). This is compensated by a reduction of the BSI to 3.8 Sv, which, because of the properties of the advected Atlantic water, leads to a cooling and freshening of the Barents Sea (mean flow and salinity are shown in Figure 9). The transport in the East Greenland Current (EGC) remains about the same, but more heat is returned from the Arctic via this current. This is consistent with the stronger and warmer WSC as some of this inflow recirculates near Fram Strait and contributes to the EGC outflow. The net result is that the total North Atlantic to Arctic heat transport decreases in response to lowered viscosity, with the larger heat transport in the WSC more than compen-

Table 2. Ocean Transports for Different Transects that Surround the Arctic Ocean[a]

Case	LOWVISC	CONT	Observed
CAA heat	3.6	1.9	
BSI heat	49	74	
WSC heat	26	8	
EGC heat	−14.6	−8.9	
Bering heat	1.4	−1.7	
Total	65.4	73.3	
CAA volume	−0.7	−0.3	−1
BSI volume	3.8	4.7	2
WSC volume	1.1	0.3	1.5
EGC volume	−5.7	−5.6	−3.5
Bering volume	1.5	0.9	0.8

[a]A positive value represents a volume or heat transport into the Arctic. Heat transport is referenced to 0°C (in TW). The volume transport is given in Sv. The observations are based on *Rudels and Friedrich* [2000].

sated for by reduced heat influx through the Barents Sea and larger heat outflow in the EGC.

[41] Transports are also changed for the other transects that define the Arctic Ocean. With reduced viscosity, the inflow through Bering Strait increases from 0.9 to 1.5 Sv. The waters entering through this Strait are also warmer and the combination of a warmed and strengthened inflow results in a heat transport increase of 3 TW. Similarly, the transports of volume and heat through the Canadian Arctic Archipelago (CAA) are increased as well.

[42] The net result of these transport changes is that in response to lowered viscosity the Arctic ocean receives less heat, with the decrease in North Atlantic heat inflow overwhelming the increase in Pacific and CAA heat inflow. This net change in heat transport is balanced by a decrease in the net surface heat loss over the Arctic domain with other factors, such as changing ice mass transport, being negligible. The reduced surface heat loss in LOWVISC is largely confined to the region just east of the BSI transect, which is due to an increase in ice cover there (Figure 5). This increased sea-ice cover is more consistent with observed sea ice conditions [see *Cavalieri et al.*, 1997; *Holland et al.*, 2006]. In turn, the increased sea ice cover in LOWVISC reduces the surface fluxes.

[43] The changes in Atlantic inflow also modify the downstream temperature profiles within the Arctic basin (Figure 10). In particular, the core of the Atlantic layer (100–1000 m) is deeper and warmer in LOWVISC, which exacerbates an already too-warm bias in the CONT. However, at depth (below 2000 m) LOWVISC is in excellent agreement with observations, whereas CONT has a warm bias. It is difficult to attribute causes to these changes unequivocally, because the Atlantic source waters, the sea-ice distribution and the surface fluxes have all changed. There is good reason to believe, though, that the good agreement at depth is due to the absence of ventilation. Thus the water still bears the signature of the observed
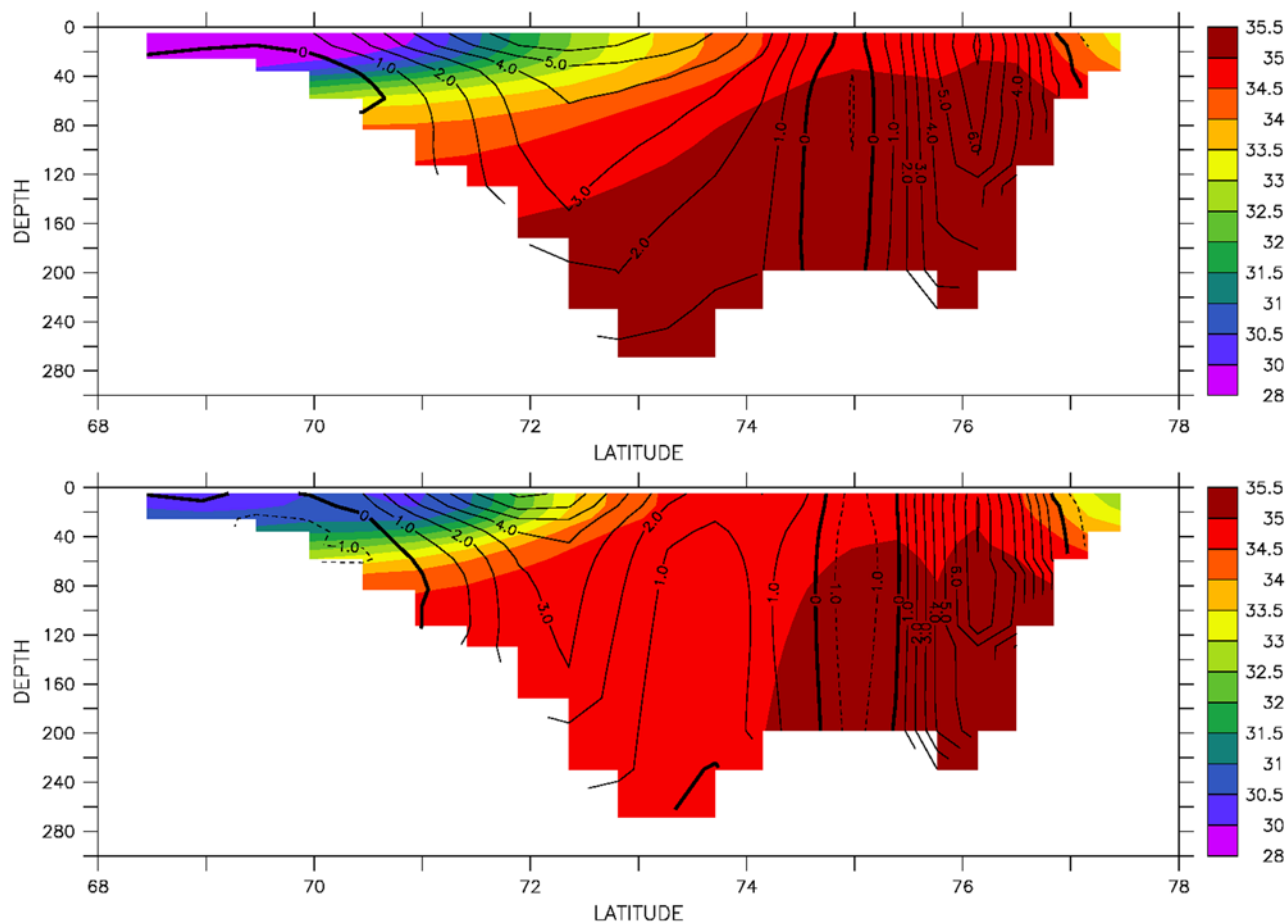
Figure 9. Salinity (in psu) and velocity (contour interval is 1 cm s^{-1}) across the Barents Sea between Spitsbergen (at 78°N) and Asia (68°N), for CONT (top), and LOWVISC (bottom).
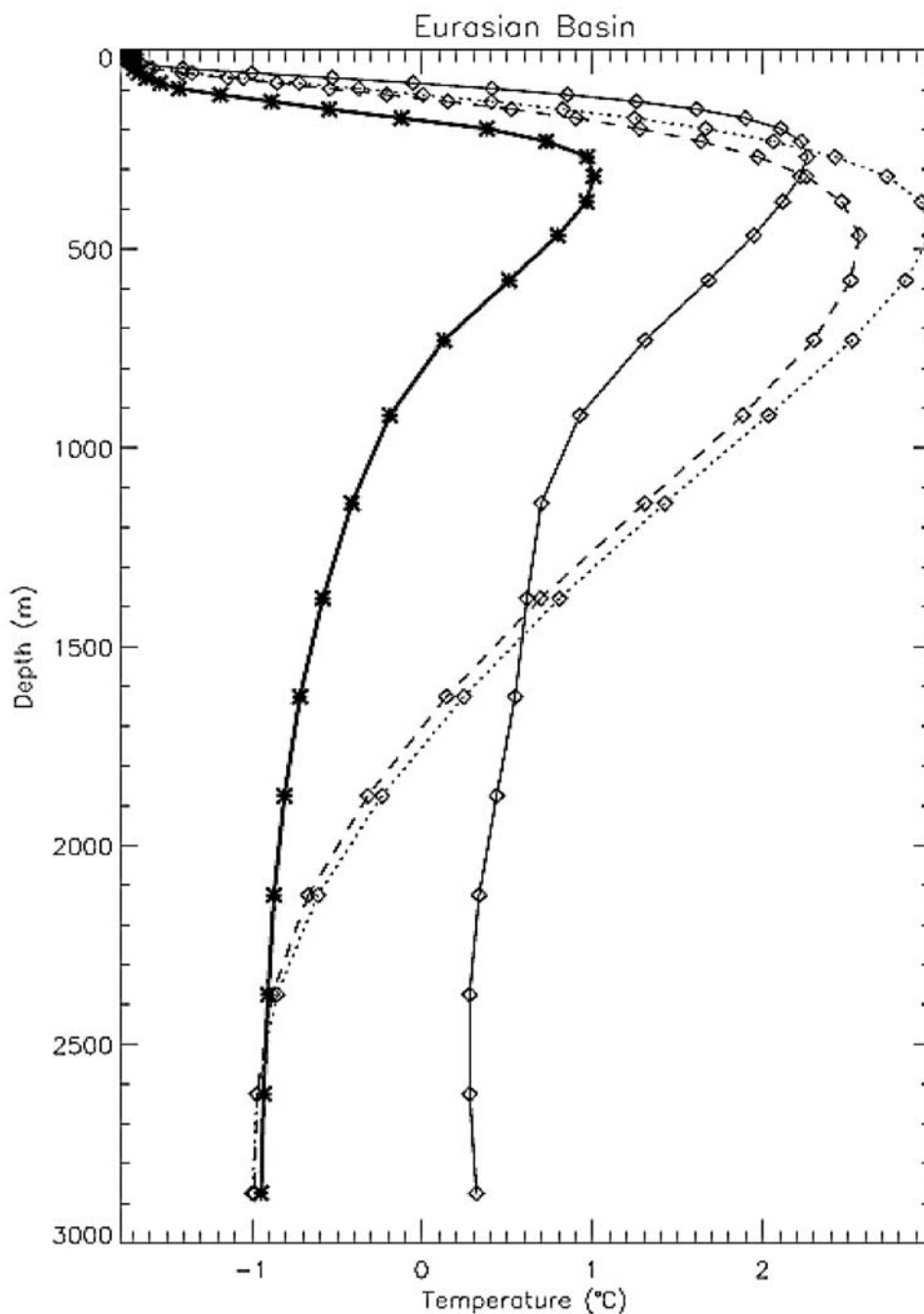
Figure 10. Temperature profiles averaged over a Eurasian Basin region for observations [*Steele et al.*, 2001; thick solid line], CONT (thin solid line), LOWVISC (dotted line), and NOSMAG (dashed line).

water mass properties with which the model is initialized. This is supported by the ideal age fields, which show that in LOWVISC, at an age of 95 years, the water at the bottom of the Eurasian basin is 20 years older than in CONT (not shown). With the caveat that the experiments are only 120 years long, the age in LOWVISC is closer to the observed age of approximately 250 years [*Schlosser et al.*, 1997] than the age in CONT. Since the Arctic basin is isolated from the adjacent basins below a depth of 900 m, one can conclude that Barents Sea convection reaches deeper in CONT than in LOWVISC. This is also consistent with the reduced import of Atlantic salt (Figure 9). The different properties

of the Atlantic layer are also likely to be due to the changed path of the Atlantic inflow. The BSI is closed below depths of 200 m, but the differences between LOWVISC and CONT in Figure 10 appear below that depth. Thus it is reasonable to conclude that the increased temperature in the Atlantic layer of LOWVISC is due to the stronger WSC which supplies the water below 200 m depth.

[44] The analysis in the present section suggests that Arctic climate and sea-ice distribution is rather sensitive to where the warm and salty Atlantic water enters the Arctic ocean. However, the flow around Spitsbergen and its variability is neither well observed, nor understood. This
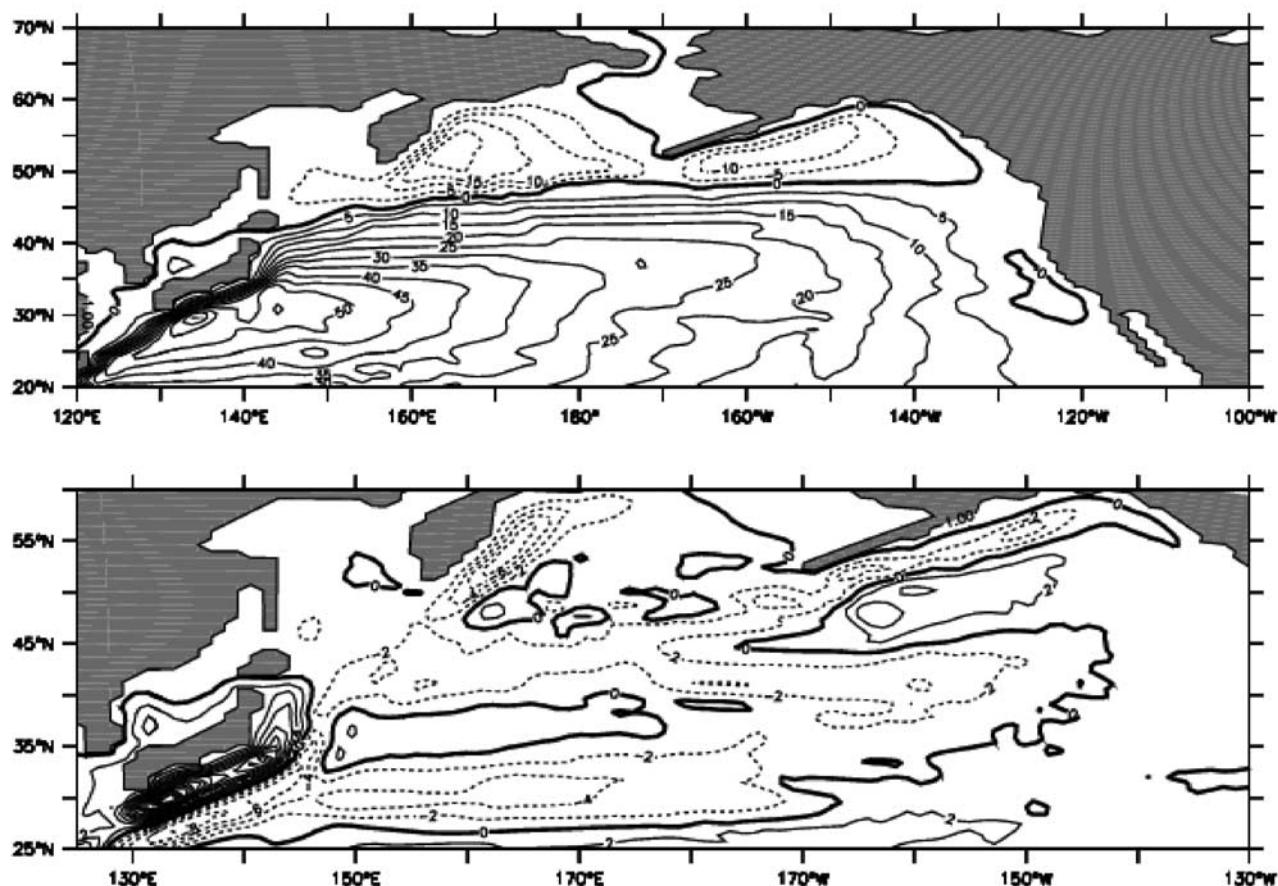
Figure 11. Vertically integrated mean volume transport in (top) LOWVISC, and (bottom) its difference from CONT (note the reduced domain to magnify details). Contour intervals are 5 Sv for the mean and 2 Sv for the difference.

is rather unfortunate and should lead to increased research efforts given the importance that Arctic sea-ice has in the current discussions about global warming [e.g., *Serreze et al.*, 2007].

7. The North Pacific

[45] Figure 4 shows four sub-regions in the North Pacific with large amplitude SST changes, namely the Kuroshio Extension, East Sea (Sea of Japan), Central North Pacific, and Bering Sea. Most of these regions coincide with the regions of large SST biases as well as Sea Surface Salinity (SSS) biases when compared with observations [*Large and Danabasoglu*, 2006]. The SST changes are mainly due to changes in the ocean circulation associated with sharpening of the coastal or frontal jets as readily found in the barotropic stream function (Figure 11). Because the SST changes are primarily driven by the circulation changes, they are colocated with SSS changes (not shown).

[46] The Kuroshio Extension in observations and eddy-resolving models is characterized by a double zonal front with a stronger eastward jet along 35°N and a secondary one near 42°N between the east coast of Japan and the dateline [*Nakamura and Kazmin*, 2003; *Nonaka et al.*, 2006]. The two fronts are often referred to as the Kuroshio and Oyashio front, respectively [*Kawai*, 1972].

The simulated Kuroshio Extension in CONT exhibits a much broader single jet that spans the latitude band between 30° and 40°N (Figure 12). This is a typical shortcoming found in GCMs with similarly resolved OGCMs. The Kuroshio Extension in NOSMAG and LOWVISC has a double jet structure with much narrower and stronger jet cores (Figures 11 and 12). The sharpening of the primary jet around 35°N is caused by the improved narrower upstream Kuroshio concentrated along the continental shelf and realistic separation near the southeastern corner of Japan. The narrower jet results in reduced eastward velocity between 35° and 40°N (dashed curve in Figure 12, right panel), which in turn causes negative SST anomalies greater than 1°C in the Kuroshio Extension south of 40°N (solid curve in Figure 12, right panel). The intensification of the northern jet and associated SST warming north of 40°N are driven by the stronger flow from the East Sea to the North Pacific through the Tsugaru Strait near 41.5°N, 141°E. The volume transport through the Tsugaru Strait increased from 0.8 Sv in the CONT to 2.4 Sv in the LOWVISC. The observed mean volume transport is about 1.5 Sv with variations between 0.8 and 2.7 Sv [*Ito et al.*, 2003]. It should be emphasized here that, when discussing transports through narrow straits, our focus is on sensitivities and not improvements, because
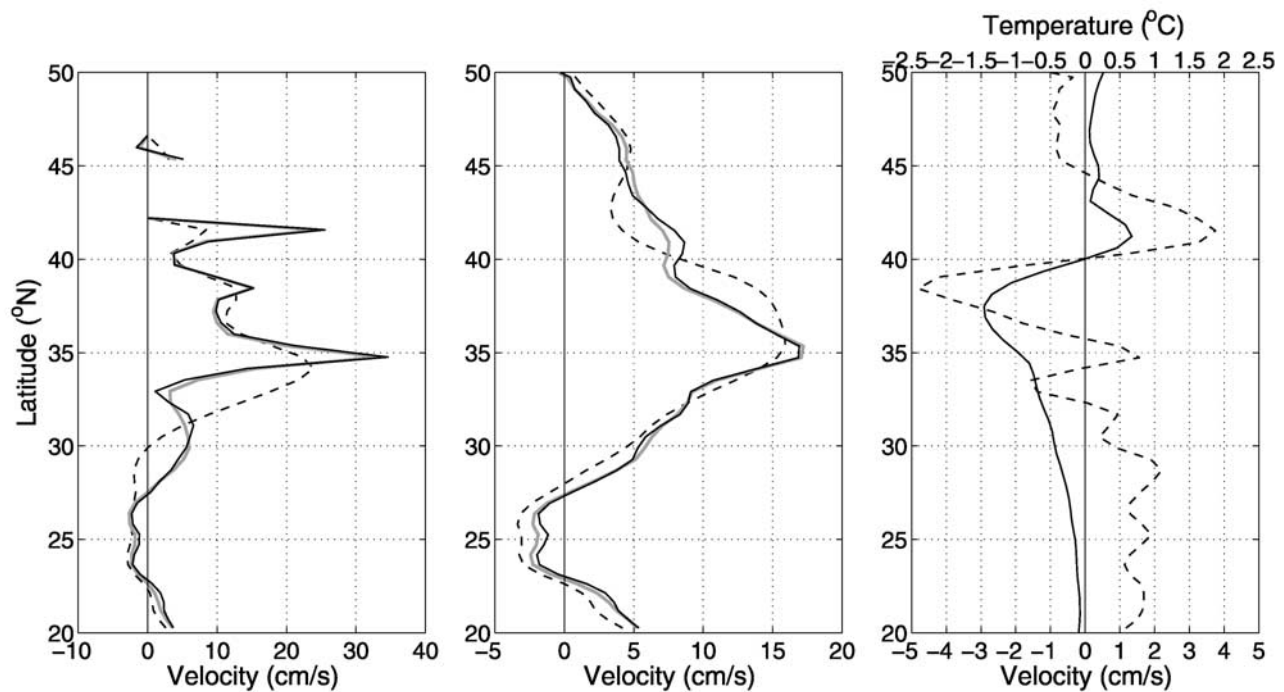
Figure 12. (left) Annual mean surface zonal velocity along 143°E from CONT (dashed), NOSMAG (thick gray solid), and LOWVISC (thin black solid). (center) Same as left but along 150°E. (right) Difference between LOWVISC and CONT along 150°E for surface zonal velocity (dashed) and SST (solid, top axis).

narrow straits in OGCMs are routinely widened to allow for a realistic throughflow.

[47] Warming in the southern half and cooling in the northern half of the East Sea are due to increased volume and heat transport from the North Pacific into the East Sea through the Korea/Tsushima Strait (near 35°N, 130°E) (Figure 11). The volume transport increased from 1.7 Sv in CONT to 3.8 Sv in the LOWVISC which caused SST warming larger than 2°C in the southern half of the East Sea (Figure 13). Observed mean volume transport through the Korea/Tsushima Strait is about 2.5 Sv with seasonal variation between 1.6 and 3.4 Sv from a 3-yearlong observation using a submarine cable [*Kim et al.*, 2004]. The volume transport change can be traced upstream to the east of Taiwan where the Kuroshio enters the East China Sea. Observations suggest that the mean volume transport of the Kuroshio east of Taiwan near 23°N is composed of about 23 Sv to the west of the Ryukyu Islands, and 12 Sv of transport east of the Ryukyu Islands [*Ichikawa and Beardsley*, 1993; *Johns et al.*, 2001]. The model cannot distinguish the two components and the sum of the two components is decreased from 43.8 Sv in the CONT to 36.3 Sv in LOWVISC, in better agreement with the observations. Note that the maximum transport of the Kuroshio does not change, rather the decrease reflects a local change due to the tighter recirculation gyre with the center of the gyre in LOWVISC being northwest of the gyre in CONT. Volume transport of the branch of the Kuroshio entering the marginal seas west of Kyushu (along 32°N between 122° and 130°E) is increased from 2.4 Sv in

CONT to 5.4 Sv in LOWVISC, which is more consistent with the observed transport of 4–5 Sv [*Ichikawa and Beardsley*, 1993; *Lie et al.*, 1998].

[48] Apart from the changes associated with the Kuroshio, there is also a noticeable warming of the Bering Sea and the Gulf of Alaska, both of which can be attributed to a strengthening of the gyres in the respective regions, as well as an increased supply of heat from the Kuroshio (Figures 11 and 13). Rather than discussing these particular two regions in detail, we defer the discussion to the next section where the Labrador Sea is used as an example for changes in northern marginal seas.

[49] Surface heat flux and rainfall anomalies between LOWVISC and CONT coincide closely with those of SST (Figure 13). As expected, SST changes are accompanied by surface heat flux changes of opposite sign, e.g., warm SST anomalies with greater heat loss to the atmosphere. This suggests that the SST changes originate in the ocean (as examined already) and the heat flux acts to dampen the SST changes. It is noteworthy that ocean induced heat flux changes are large enough to force a change in the winds and hence the wind stress curl (Figure 13, bottom). These changes are confined to the area of the SST anomalies and are consistent with the results of earlier studies that show how midlatitude SST anomalies set up pressure field anomalies which induce surface wind changes [*Alexander et al.*, 2006; *Kwon and Deser*, 2007]. For orientation, the wind curl changes are of the same magnitude as the changes that can be
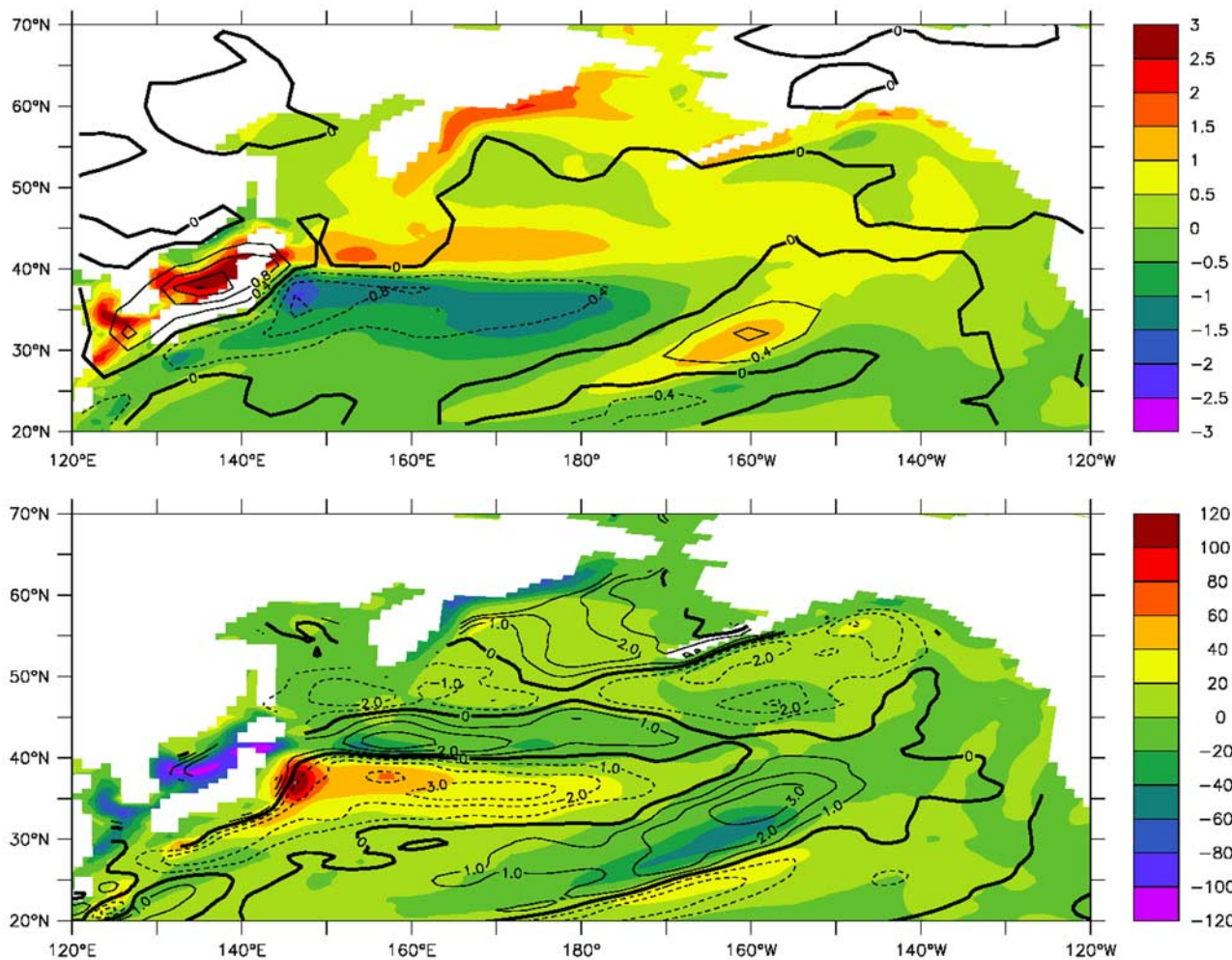
Figure 13. Difference between LOWVISC and CONT in (top) SST (color) and precipitation (contourlines: 0.4 mm/d, maximum: 1.6 mm/d); and (bottom) in net surface heat flux (color) and wind stress curl (contourlines: 1×10^{-8} Nm^{-3}).

expected from a one standard deviation event of the Pacific Decadal Oscillation.

8. The Labrador Sea

[50] Among the largest effects of lower viscosity are the warmer surface temperatures (Figure 4) and reduced sea-ice (Figure 5, consistent with MOM) in the Labrador and Bering Seas. These sub-polar marginal seas lose significant heat through their surface, which is balanced primarily by advection by the model's resolved flow. Much of this advection occurs in boundary currents near the coasts where the deformation due to the shear imposed by the no slip boundary condition produces significant Smagorinsky viscosity. Therefore most of the LOWVISC signals are seen in NOSMAG, which will be the basis of most of the comparisons with CONT. In this section we will discuss in detail the changes to the Labrador Sea as an example for northern marginal seas.

[51] Temperature and velocity in the Labrador Sea at 50 m depth are shown in Figure 14, from both CONT and NOSMAG. Also shown are the contours of 5 and 50% mean sea-ice concentration. As expected, the boundary currents off east Greenland, west Greenland and Labrador are much stronger in NOSMAG. However, the region centered at about 67°N, 330°E appears to be a notable exception. Although small, this region contains a pool of cold water that is less than −1°C at 50 m. In CONT this water can be traced along the coast, past Cape Farewell and into the Labrador Sea. In contrast, the weaker NOSMAG flow in the region cannot transport as much of this water in the face of stronger currents that carry a greater proportion of warm, salty water from the Irminger Sea. The net result is a warmer and stronger boundary current entering the Labrador Sea south of Cape Farewell. The associated greater heat transport warms most of the Labrador Sea above about 1000 m depth, and the near surface heat advection and mixing cause the sea-ice to retreat in better agreement with observations. To the north-west, the 5% concentration contour is displaced by about 600 km, while off Labrador it lies only about one-half the distance offshore. Note that in NOSMAG, in contrast to CONT, the area of observed convection (centered at 54°W/58°N [Pickart et al., 2002]) is in open water, fulfilling now the necessary condition for convection.
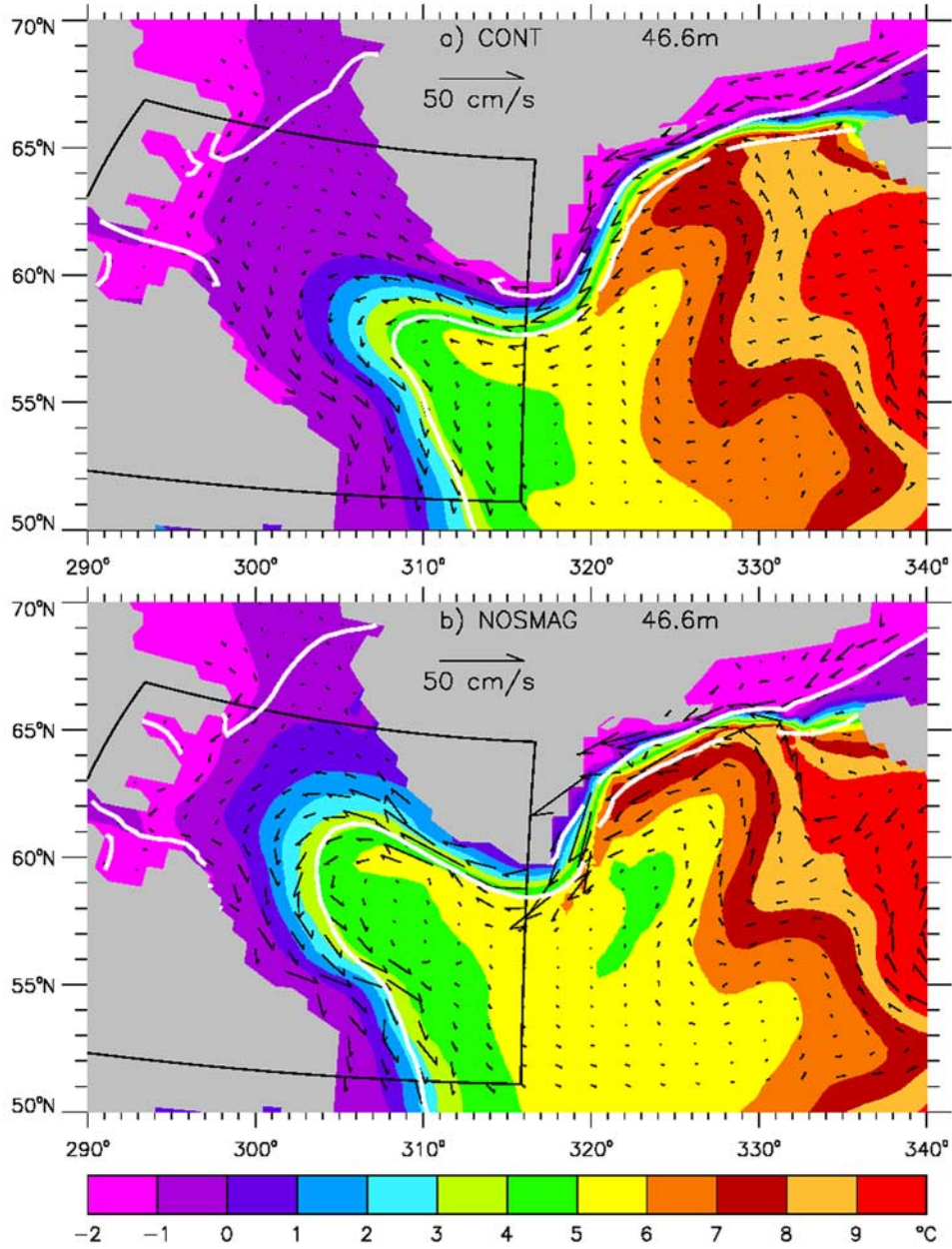
Figure 14. Temperature and velocity at 50 m depth for CONT (a) and NOSMAG (b). The 5% and 50% sea ice concentration contours are shown in white, with the smaller always more offshore. The heat budget is computed for the region inside the box.

[52] To understand the changes in more detail it is helpful to analyze the heat budget over the domain in the box shown in Figure 14:

$$AH_W + AH_E + AH_S + AH_N = -\overline{Q}$$

where on the left-hand-side the four terms are the advection of heat through the western, eastern, southern and northern side of the box, as defined in Appendix B. The sum of these terms is the total heat advection, *AH*, which is balanced on the right-hand-side by surface heat loss through the surface. A further consideration that crudely incorporates the insulating effects of sea-ice is to neglect mean ice-ocean heat exchange and to define an effective air-sea heat flux, Q_{as}, such that:

$$\overline{Q} = (1 - f_{ice})Q_{as},$$

where f_{ice} is the mean fractional ice coverage. By extending a domain to the ocean bottom, AH_B becomes zero and assuming steady state of the twenty years $101-120$ the heat budget simplifies to

$$AH = AH_W + AH_E + AH_S + AH_N = -\overline{Q} = -(1 - f_{ice})Q_{as}.$$

Table 3. Heat Budget of the Labrador Sea in CONT, NOSMAG and LOWVISC[a]

	CONTROL	NOSMAG	LOWVISC
AH_E	477	572	584
in-out	551−74	738−166	770−186
AH_S	−447	−518	−528
in-out			
AH_{N+W}	−3	−5	−5
AH	27	48	50
Q_s	−25	−47	−51
Q_{as}	−36	−60	−62
f_{ice}	0.30	0.17	0.17
SST(°C)	1.3	2.5	2.7

[a]Except for sea ice concentration, f_{ice} (fraction of 1), and SST, all entries are in Wm^{-2} equivalents over the surface sea area of 1.6×10^6 km^2.

[53] The steady state response to lower viscosity, as inferred above, is heating from the left hand side until it becomes balanced by increased surface heat loss, which can result from either more negative net air sea heat flux, Q_{as}, or less sea-ice concentration, f_{ice}.

[54] The terms of the heat budget for the Labrador Sea box are summarized in Table 3. The simple budget, $AH = -\overline{Q}$, of the heat budget above is closed to within 1 Wm^{-2}, justifying the neglect of sea ice - atmosphere heat flux. Most of the lower viscosity signals of Table 3 are captured in NOSMAG, and the even lower viscosity of LOWVISC continues the trend in all measures. Unlike the sum AH, its components (Appendix B) cannot be interpreted as an equivalent surface flux, because they depend on the non-zero mass flux through the particular domain face, and hence on the temperature unit, Celsius or Kelvin. However, differences in these terms between experiments are meaningful relative measures of heat budget changes.

[55] With these preparations one can now understand how viscosity changes the heat budget in detail. The biggest difference is in the inflow across the eastern face, which, as suggested by Figure 14, is due both to a stronger boundary current inflow and warmer temperatures with lower viscosity. The associated additional volume flux mainly flows out across the southern face and makes AH_S more negative despite warmer temperatures. The warmer temperatures increase the heat outflow across the eastern face and, to a much less degree, the northern and western passages. However, the total increase in outflow falls short of the difference in eastern inflow by the 22 to 24 Wm^{-2} increase in AH. The extra heating warms the SST by 1.2 to 1.4°C before becoming balanced by more surface cooling (more negative $\overline{Q}$). This cooling is due to two factors: the loss of nearly half the sea-ice cover from 30% to 17%, and a more negative Q_{as} in response to the warmer SSTs. This response gives an air-sea coupling strength of about 18 Wm^{-2} per °C, which is about half of that expected from SST alone and similar to the *Doney et al.* [1998] global estimate of 14.6 Wm^{-2} per °C from an earlier coupled model.

[56] An ancillary experiment was performed to demonstrate the mechanisms by which viscosity affects the Labrador Sea. Starting from year 100 of NOSMAG, a twenty year integration was performed with CONT viscos-

ity so that the transient response to Smagorinsky viscosity could be observed in the Labrador Sea. This response is shown in Figure 15, as monthly mean differences from NOSMAG in horizontal velocity and temperature at a model depth of 50 m. The velocity response is rapid, with most of the differences with NOSMAG fully evident in the first monthly mean from January year 100 (Figure 15a). The large increase in viscosity immediately decelerates the currents offshore of the Labrador, West Greenland and East Greenland coasts. The currents have changed from being similar to those in Figure 14a, to being much like Figure 14b in much less than a month. Of particular note is the loss of the near zonal flow at 55°N off Labrador in Figure 14b, and the strength of the convergence to the west of Iceland.

[57] This convergence produces the strong east-west temperature front seen to the west of Iceland in Figure 14. With increased viscosity the front shifts to the north and produces the 4°C Denmark Strait warming seen in Figure 15a. The higher viscosity also appears to shift the north-south temperature front between 64°N and Cape Farewell farther from the east Greenland coast, such that there is a local 2°C cooling in Figure 15a. By February a similar frontal shift offshore off West Greenland results in another cool spot (not shown). Over the next several months these patches continue to develop larger differences from NOSMAG and the new currents advect the signals in the boundary currents. By July (Figure 15b) there is a large area of greater than 5°C Denmark Strait heating, and of more than −3°C cooling off both the west and east Greenland coasts. The cold anomaly of the latter and its downstream advection are reduced during the following months by advection of the Denmark Strait warm anomaly, so that by January year 101, the maximum cold difference (−4°C) is found off west Greenland (Figure 15c), and the signal has propagated all along the Labrador coast. Also by this time warm differences have developed south of Iceland at 60°N, east of Cape Farewell at 321°E and off Newfoundland at 312°E. Thus after only 1 year the transient response is essentially complete, with Figure 15c a very good representation of the differences in the 20 year mean of Figure 14.

[58] The stronger coastal circulation due to the reduced viscosity clearly improved the sea-ice conditions in the Labrador Sea. As in the Arctic Ocean, though, it is not obvious to what extent the representation of the ocean has improved. However, in the Labrador Sea there are more observations available by which to judge the results. The strength of the Labrador Gyre increased from 44 Sv in CONT to 60 Sv in NOSMAG and to 62 Sv in LOWVISC. The observations by *Johns et al.* [1995] and *Pickart et al.* [2002] suggest 48 and 40 Sv, respectively. Thus the new Labrador Gyre is too strong. However, like in the case of the ACC, the uncertainties in the observations and the surface forcing provided by the coupled model make it difficult to judge the changes by the transport alone. Dynamically more meaningful is the actual width of the currents. Observations [*Niiler et al.*, 2003] show that strong flow in the Labrador Sea is confined along the coast and reaches deep into the northwestern Labrador Sea, which is
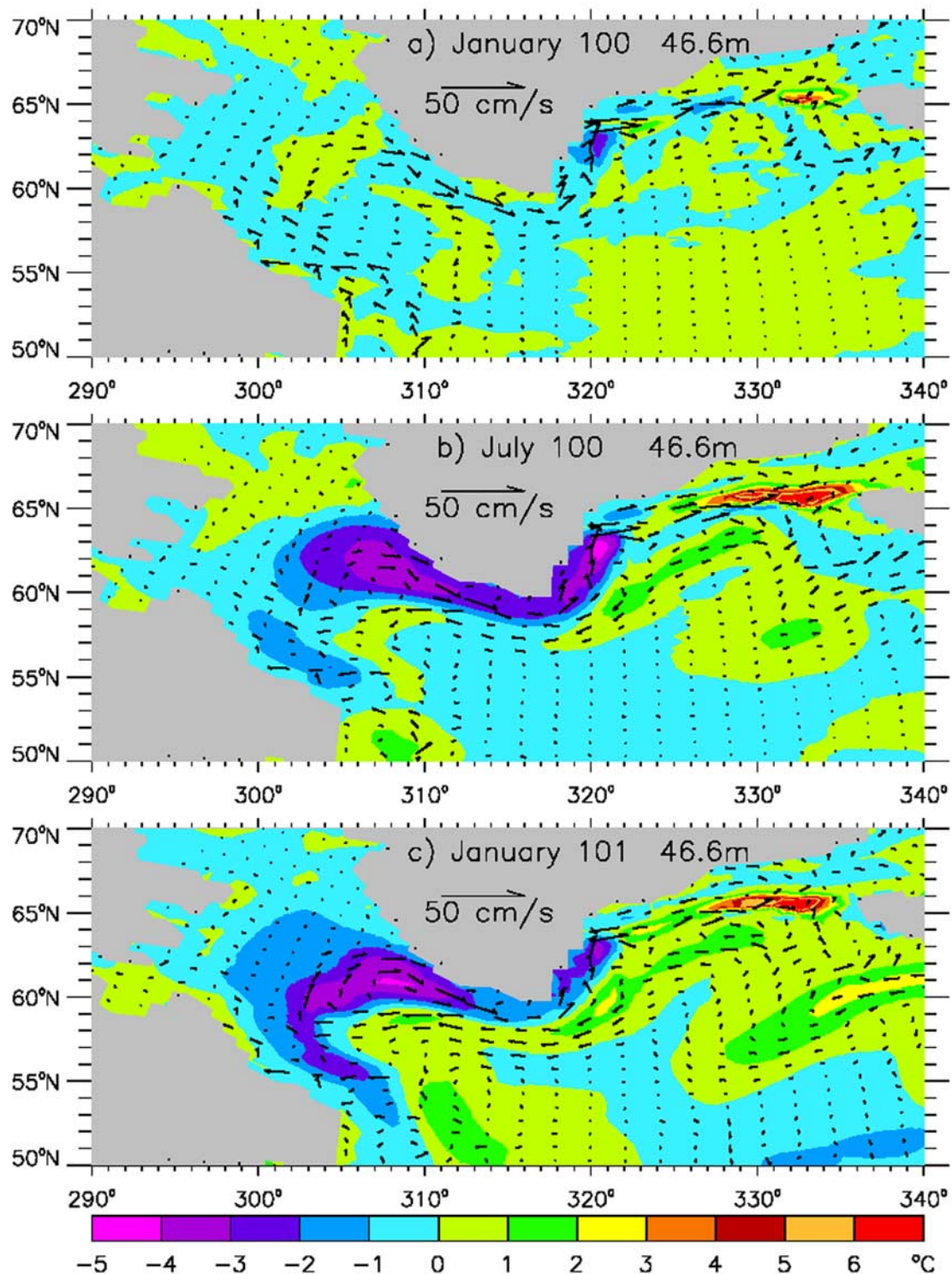
Figure 15. The changes in temperature and velocity at 50 m depth directly after Smagorinsky viscosity has been switched on in NOSMAG. (a) After one month; (b) after seven months and (c) after one year.

also the case in NOSMAG (Figure 14) and LOWVISC (not shown), but not in CONT where the flow is sluggish and spread across the whole Labrador Sea.

[59] It should be noted that the arguments presented here are strictly local: the sea-ice distribution improved because the coastal currents improved. However, the North Atlantic subpolar gyre is adjacent to the North Atlantic Current whose path around the Grand Banks is notoriously difficult to simulate [e.g., *Smith et al.*, 2000]. Thus one cannot rule out the possibility that improving the Gulf Stream also

improves the sea-ice distribution, without the need of improved Labrador Sea circulation.

9. Summary and Discussion

[60] The impact of parameterized ocean viscosity on global climate is explored with three 120-year integrations of CCSM3, a state of the art coupled climate model. It is found that reducing viscosity leads to a generally improved ocean circulation at the expense of an increase in numerical noise. The large-scale atmospheric circulation does not change noticably. The major ocean improvements are:

[61] • In the equatorial Pacific the emergence of TIWs reduces the cold tongue bias common to many GCMs including CCSM3.

[62] • The ACC becomes narrower and weakens by 20%, making it more realistic on both counts.

[63] • The improved representation of the Atlantic inflow into the Arctic Ocean leads to an improved sea-ice distribution there.

[64] • The improved path of the Kuroshio leads to an improved temperature and salinity distribution across the midlatitude Pacific.

[65] • Reduced viscosity allows for a more realistic representation of the coastal currents in the Labrador Sea and removes a long standing bias of excessive sea-ice.

[66] Based on these results we conclude that for OGCMs numerical stability criteria only provide a starting point in the iterative search for an optimal viscosity. Experimenting with the details may carry one beyond what is considered proper from the numerical point of view, but can lead to an overall superior solution. It appears that what is needed is a systematic exploration of the dependencies between viscosity, topography, resolution and noise. There are no hard rules on how much noise is acceptable in OGCMs (see, however, *Griffies et al.* [2000] for a lucid discussion on some of the issues). Substantial noise exists even in a solution that obeys most numerical criteria (see CONT in Figure 2), simply because noise is not only created by numerical instabilities, but also by flow over small scale features in the model topography from where it radiates into the general circulation. Thus "the desire to model the complex, rough ocean bottom and coastline of physical reality is in competition with the simple, smooth topography needed to assure numerical accuracy" [*McWilliams*, 1996]. It should be noted that it is already common practice to artificially widen or deepen straits in OGCMs to ensure realistic throughflow. In POP, for example, the Florida Strait and the Korea/Tsushima Strait are deeper and wider than observed. One could argue that now, after adopting reduced viscosity, the Korea/Tsushima Strait transport is too large (section 7) and the strait should be made shallower again.

[67] Ignoring numerical constraints and reducing viscosity created a simulation that raises some physical questions, and highlighted sensitivities of climate relevant ocean processes:

[68] • The flow around Spitsbergen may be weak but has to be better understood before sea-ice predictions in climate warming scenarios can be made with confidence.

[69] • The strong dependence of the ACC transport on viscosity, especially the inverse relation between transport

and kinetic energy, is to our knowledge not discussed in the literature. This adds another, new, element to the already complex ACC dynamics.

[70] • The momentum balance of the EUC remains an unsolved issue. After reducing viscosity TIWs should take over to remove momentum from the EUC. However, they do not remove momentum sufficiently to create the proper core depth.

[71] The response of the coupled system to lower ocean viscosity depends on regional SST changes. Therefore the general result that the large scale atmospheric circulation barely responds to significant oceanic improvements, although disappointing, is thoroughly consistent with the present understanding of air-sea interaction: Large scale atmospheric changes can only be expected through convective anomalies triggered by SST anomalies in tropical warmpools [e.g., *Palmer and Mansfield*, 1984]. As shown here, however, the warmpools are not affected significantly by viscosity. One the other hand, temperature changes in the Arctic Ocean and subpolar gyres can trigger sea-ice responses and a large ice-albedo feedback, which suggests that the coupled system in the ice covered oceans is more sensitive to changes in ocean parameterizations than the convectively active tropical oceans. It should be kept in mind, though, that the high-latitude oceans have strong horizontal and weak vertical temperature gradients, whereas the opposite is true for the tropics. Thus horizontal mixing process should have a relatively larger impact in the high latitudes, whereas vertical mixing process should be more relevant for the tropics. Reassessing the values and impacts of vertical mixing will be addressed in future research.

Appendix A: Anisotropic Horizontal Viscosity

[72] The horizontal viscosity is anisotropic, following *Large et al.* [2001], as generalized and discretized by *Smith and McWilliams* [2003] for any orthogonal horizontal (x-y) grid with cell dimensions (Δx, Δy). The parameterization appears in the prognostic equation for the respective horizontal velocity components, U and V, and requires two coefficients A and B. In general these coefficients can vary in space and time. The stress tensor is proportional to horizontal shears and is zero in the case of solid body rotation.

[73] In the special case of spatially uniform coefficients in Cartesian coordinates the friction is given by

$$F_x = A\partial_x^2 U + B\partial_y^2 U - \frac{1}{2}(A - B)\partial_x\left(\vec{\nabla}_H \cdot \vec{U}\right), \quad (A1)$$

$$F_y = B\partial_x^2 V + A\partial_y^2 V - \frac{1}{2}(A - B)\partial_y\left(\vec{\nabla}_H \cdot \vec{U}\right). \quad (A2)$$

The terms involving gradients of horizontal divergence ($\vec{\nabla}_H \cdot \vec{U}$) are small with little influence on solutions, but are added following *Smith and McWilliams* [2003] to ensure that the viscous terms are purely dissipative of kinetic energy, for $\{A, B\} > 0$, and not just $A > B > 0$ as in the work of *Large et al.* [2001]. Examination of equations (A1) and (A2) reveals that the A coefficient acts in the direction parallel to the flow component, while B acts perpendicular.

[74] There are three possible choices for breaking isotropy with different A and B, i.e., alignment choices. In the first (ALIGN = GRID), the flow components are the prognostic U and V. In the second option (ALIGN = E−W), the effective flow components of (A1) and (A2) become the zonal and meridional velocities. In unrotated, spherical coordinates, these two alignment choices are equivalent. In the third option (ALIGN = FLOW), the effective components are downstream and cross-stream. Option (ALIGN = E−W) is the default in POP and is used for all the present experiments. For a latitude-longitude grid at the equator the three options are nearly equivalent near the surface, because the dominant flow is zonal in the x-direction. From equation (A1), maintenance of this current structure requires low values of B [*Large et al.*, 2001].

[75] Some ocean physics is thought to be represented by coefficients $\{A, B\}_{SMAG}$ that depend on the resolved model flow, while physics that is entirely sub-grid scale (SGS) requires different coefficients, $\{A, B\}_{SGS}$. In addition, viscosity must be large enough ($\{A, B\} > \{A, B\}_{NOISE}$) to suppress the generation of numerical noise on the model grid scale, and small enough ($\{A, B\} < \{A, B\}_{VCFL}$) to satisfy the viscous CFL criteria for numerical stability. In practice, it may sometimes be necessary to compromise the physics, and to tolerate some noise. Intermediate viscosity coefficients A' and B' are found

$$A' = \max[A_{SGS}, A_{SMAG}, A_{NOISE}], \tag{A3}$$

$$B' = \max[B_{SGS}, B_{SMAG}, B_{NOISE}]. \tag{A4}$$

Then, because numerical stability must be assured, the final coefficients are given by

$$A = \min[A', A_{VCFL}], \tag{A5}$$

$$B = \min[B', A_{VCFL}]. \tag{A6}$$

[76] Estimates of lateral viscosity based on observed lateral mixing [e.g., *Sundermeyer and Price*, 1998; *Zhurbas and Oh*, 2003] suggest coefficients of $\mathcal{O}(1000)$ m^2 s^{-1}, or larger, with some degree of anisotropy. However, these values only provide an upper bound on $\{A, B\}_{SGS}$, because they include contributions from model resolved flow, especially in the tropics, that do not need to be parameterized. In order to allow B_{SGS} to be small at the equator and increase poleward for latitude, ϕ, between $\pm\phi_I$, the general form for $\{A, B\}_{SGS}$ is

$$A_{SGS} = A_{eddy}, \tag{A7}$$

$$B_{SGS} = B_{eddy}[1 + C_2(1 - \cos(2\phi'))], \tag{A8}$$

where $\phi' = 90°$ min $(|\phi|, \phi_I)/\phi_I < 90°$. A_{SGS} is constant at a physical value of A_{eddy} of $\mathcal{O}(1000)$ m^2 s^{-1}, and at the equator B_{SGS} equals B_{eddy} which can be less than A_{eddy} here. A preferred option is to set $(1 + 2C_2) = A_{eddy}/B_{eddy}$, so that B_{SGS} becomes equal to A_{SGS} poleward of a midlatitude ϕ_I.

[77] Non-linear dependence of the viscosity coefficients $\{A, B\}_{SMAG}$ on the deformation rate of the resolved flow and on the model grid spacing, $ds = \min[\Delta x, \Delta y]$, is discussed by *Smagorinsky* [1993]. It is implemented as [see *Smith and Gent*, 2002]

$$A_{SMAG} = C_A D ds^2, \tag{A9}$$

$$B_{SMAG} = C_B D ds^2; C_{eq} \leq C_B < C_{lim}, \tag{A10}$$

where the coefficient C_B is a function of latitude and is set to a low value, C_{eq}, equatorward of $|\phi| = 20°$. At higher latitudes, C_B increases exponentially toward an upper limit of C_{lim}, as given by

$$F(\phi) = C_{lim} - (C_{lim} - C_{eq})e^{-\frac{(|\phi|-20)^2}{100\left[1-\frac{C_{eq}}{C_{lim}}\right]}}, |\phi| > 20°. \tag{A11}$$

The deformation rate, D, is the square root of twice the norm of the strain rate tensor, and hence is given by

$$\frac{1}{2}D^2 = (\partial_x U)^2 + (\partial_y V)^2 + (\partial_x V + \partial_y U)^2. \tag{A12}$$

[78] The strongest numerical constraint on viscosity is the viscous CFL criterion, which prevents numerical instability that can be generated when momentum diffuses through a grid cell in less than the time interval of the integration, Dt. Often Dt is the timestep, Δt, but for leapfrog schemes $Dt = 2\Delta t$. In one dimension, linear stability analysis says that the viscosity must be less than $\Delta x^2/(2Dt)$. There are different extensions for two dimensions and a conservative form is:

$$A + B < \frac{1}{4Dt}\left(\Delta x^{-2} + \Delta y^{-2}\right)^{-1} = A_{VCFL}, \tag{A13}$$

[79] *Bryan et al.* [1975] discuss two numerical noise issues that enter into $\{A, B\}_{NOISE}$. First, the grid Reynolds number should be less than 2, so that noise advected into a grid cell is effectively diffused. Using this criterion, we define an associated minimum viscosity as

$$A_{GRe} = \frac{1}{2}V_s(\phi)e^{z/1000}\max[\Delta x, \Delta y], \tag{A14}$$

where $-z$ is depth and $V_s(\phi)$ is a characteristic surface velocity that is 0.15 m s^{-1} poleward of 30°, and increases to 1 m s^{-1} at the equator according to

$$V_s(\phi) = 0.425\cos\left(\frac{\phi\pi}{30}\right) + 0.575, \text{ for } |\phi| < 30°. \tag{A15}$$

Second, the width of viscous western boundary layers [*Munk*, 1950] must exceed the grid spacing in the offshore direction, Δx, which leads to another minimum viscosity

$$B_{MUNK} = 0.16\beta\Delta x^3 e^{-p(x)^2} \tag{A16}$$

where to the east of all solid boundaries, $p(x)$ equals 1 for three grid points east then falls off exponentially

with an e-folding distance of 1000 km and $\beta = 2.28 \times 10^{-11}$ m^{-1} s^{-1} cos(ϕ).

Appendix B: The Heat Budget on the Model Grid

[80] Over a time Δt, the heat content per unit volume, H, of a model grid cell of dimensions Δx, Δy, Δz, respectively in the model's orthogonal x, y, z grid directions, changes according to:

$$\frac{\Delta H}{\rho C_p \Delta t} = - \partial_x[UT] - \partial_y[VT]$$
$$- \partial_z[WT] - \partial_z[w'T'] + \text{other terms}, \quad (B1)$$

where U, V and W are the respective velocity components, $[w'T']$ is the parameterized vertical flux due to the unresolved flow, T is potential temperature, and ρC_p is the product of ocean density and heat capacity. Neglecting the other terms such as resolved and unresolved lateral eddy fluxes, this equation is discretized as:

$$\frac{\Delta H}{\rho C_p \Delta t} = \frac{[UT]_w - [UT]_e}{\Delta x} + \frac{[VT]_s - [VT]_n}{\Delta y} + \frac{[WT]_b - [WT]_u}{\Delta z}$$
$$+ \frac{[w'T']_b - [w'T']_u}{\Delta z} \quad (B2)$$

where subscripts w, e, s, n, b and u indicate grid box faces in the decreasing x (west), increasing x (east), decreasing y (south), increasing y (north), decreasing z (down) and increasing z (up) directions, respectively. The respective faces of a large domain of surface area A_D are denoted W, E, S, N, B, U.

[81] When summed over such a domain, denoted as Σ_D, contributions at interior grid faces cancel, so that only the terms from these domain faces remain:

$$A_D^{-1} \Sigma_D \left(A dz \frac{\Delta H}{\Delta t} \right) = AH_W + AH_E + AH_S + AH_N + AH_B + \overline{Q}, \quad (B3)$$

where the factor A_D^{-1} converts the heat energy changes into an equivalent surface heat flux over the domain and $\overline{Q}$ is the average surface heat flux. The contributions across each of the domain faces, excluding the surface where the term is identically zero, are given by:

$$AH_W = A_D^{-1} \Sigma_W \left(\rho C_p \left[\frac{UT \Delta y}{A} \right]_w A \Delta z \right) \quad (B4)$$

$$AH_E = A_D^{-1} \Sigma_E \left(-\rho C_p \left[\frac{UT \Delta y}{A} \right]_e A \Delta z \right) \quad (B5)$$

$$AH_S = A_D^{-1} \Sigma_S \left(\rho C_p \left[\frac{VT \Delta x}{A} \right]_s A \Delta z \right) \quad (B6)$$

$$AH_N = A_D^{-1} \Sigma_N \left(-\rho C_p \left[\frac{VT \Delta x}{A} \right]_n A \Delta z \right) \quad (B7)$$

$$AH_B = A_D^{-1} \Sigma_B \left(\rho C_p \left[\frac{WT}{\Delta z} \right]_b A \Delta z \right), \quad (B8)$$

where all the terms in square brackets from each model time step are summed before any averaging. It is possible to partition each of these terms into inflow and outflow components, according to the sign of the velocity component. This procedure was not performed each time step, so it can only be approximated by using the mean (usually monthly) velocities.

References

Alexander, M., J. Yin, A. C. G. Branstator, C. Cassou, R. Cullather, Y.-O. Kwon, J. Norris, J. Scott, and I. Wainer (2006), Extratropical atmosphere-ocean variability in CCSM3, J. Clim., 19, 2496–2525.

Baturin, N., and P. Niiler (1997), Effects of instability waves in the mixed layer of the equatorial Pacific, J. Geophys. Res., 102, 27,771–27,793.

Boville, B. A. (1991), Sensitivity of simulated climate to model resolution, J. Clim., 4, 469–485.

Bryan, K., S. Manabe, and R. C. Pacanowski (1975), A global ocean-atmosphere climate model. Part II: The oceanic circulation, J. Phys. Oceanogr., 5, 30–46.

Bryden, H., and E. Brady (1989), Eddy momentum and heat fluxes and their effects on the circulation of the equatorial Pacific ocean, J. Mar. Res., 47, 55–79.

Carmack, E. C. (1990), Large-scale physical oceanography of polar oceans, in Polar Oceanography, Part A: Physical Science, edited by J. Walker and O. Smith, pp. 171–222, Academic Press, Princeton.

Cavalieri, D., C. Parkinson, P. Gloersen, and H. Zwally (1997), Sea ice concentrations from nimbus-7 SMMR and DMSP SSM/I passive microwave data, 1979–1999, National Snow and Ice Data Center.

Collins, W. D., et al. (2006), The Community Climate System Model: CCSM3, J. Clim., 19, 2122–2143.

Cox, M. (1980), Generation and propagation of 30-day waves in a numerical model of the Pacific, J. Phys. Oceanogr., 10, 1168–1186.

Cunningham, S. A., S. G. Anderson, B. A. King, and M. A. Brandon (2003), Transport and variability of the Antarctic circumpolar current in drake passage, J. Geophys. Res., 108(C5), 8084, doi:10.1029/2001JC001147.

Danabasoglu, G., and J. Marshall (2007), Effects of vertical variations of thickness diffusivity in an ocean general circulation model, Ocean Modell., 18, 122–141.

Danabasoglu, G., and J. C. McWilliams (1995), Sensitivity of the global ocean circulation to parameterizations of mesoscale tracer transports, J. Clim., 8, 2967–2987.

Danabasoglu, G., et al. (2006), Diurnal coupling of the tropical oceans in CCSM3, J. Clim., 19, 2347–2365.

Deser, C., A. Capotondi, R. Saravanan, and A. Phillips (2006), Tropical Pacific and Atlantic climate variability in CCSM3, J. Clim., 19, 2451–2481.

Dickson, R., B. Rudels, S. Dye, M. Karcher, J. Meincke, and I. Yashayaev (2007), Current estimates of freshwater flux through Arctic and subarctic seas, Prog. Oceanogr., 73, 210–230.

Doney, S. C., W. G. Large, and F. O. Bryan (1998), Surface ocean fluxes and water-mass transformation rates in the coupled NCAR climate system model, J. Clim., 11, 1420–1441.

Dukowicz, J. K., and R. D. Smith (1994), Implicit free-surface method for the Bryan-Cox-Semtner ocean model, J. Geophys. Res., 99, 7991–8014.

Eden, C. (2007), Eddy length scales in the North Atlantic Ocean, J. Geophys. Res., 112, C06004, doi:10.1029/2006JC003901.

Fox-Kemper, B., and D. Menemenlis (2007), Can large eddy simulation techniques improve mesoscale rich ocean models?, in AGU Monograph Ser., vol. 157, edited by M. Hecht and H. Hasumi, in press.

Freeland, H. J., P. Rhines, and T. Rossby (1975), Statistical observations of the trajectories of neutrally buoyant floats in the North Atlantic, J. Mar. Res., 33, 383–404.

Gent, P., and J. McWilliams (1990), Isopycnal mixing in ocean circulation models, J. Phys. Oceanogr., 20, 150–155.

Gent, P. R., and J. C. McWilliams (1996), Eliassen-Palm fluxes and the momentum equation in non-eddy-resolving ocean circulation models, J. Phys. Oceanogr., 26, 2539–2546.

Gent, P. R., W. G. Large, and F. O. Bryan (2001), What sets the mean transport through Drake Passage?, J. Geophys. Res., 106, 2693–2712.

Griffies, S. M. (2004), Fundamentals of Ocean Climate Models, Princeton Univ. Press, Princeton, N. J.

Griffies, S. M., and R. W. Hallberg (2000), Biharmonic friction with a Smagorinsky-like viscosity for use in large-scale eddy-permitting ocean models, *Mon. Weather Rev.*, 128, 2935–2946.

Griffies, S. M., R. C. Pacanowski, and R. W. Hallberg (2000), Spurious diapycnal mixing associated with advection in a z-coordinate model, *Mon. Weather Rev.*, 128, 538–564.

Griffies, S. M., et al. (2005), Formulation of an ocean model for global climate simulations, *Ocean Sci.*, 1, 45–79.

Hallberg, R., and A. Gnanadesikan (2006), The role of eddies in determining the structure and response of the wind-driven southern hemisphere overturning: Results from the modeling eddies in the Southern Ocean (MESO) project, *J. Phys. Oceanogr.*, 36, 2232–2252.

Hansen, D., and C. Paul (1984), Genesis and effects of long waves in the equatorial Pacific, *J. Geophys. Res.*, 89, 10,431–10,440.

Harrison, D. E. (1978), On the diffusion parameterization of mesoscale eddy effects from a numerical ocean experiment, *J. Phys. Oceanogr.*, 8, 913–918.

Holland, W. R., J. C. Chow, and F. O. Bryan (1998), Application of a third-order upwind scheme in the NCAR ocean model, *J. Clim.*, 11, 1487–1493.

Holland, M. M., C. M. Bitz, E. C. Hunke, W. H. Lipscomb, and J. L. Schramm (2006), Influence of the sea ice thickness distribution on polar climate in CCSM3, *J. Clim.*, 19, 2398–2414.

Ichikawa, H., and R. C. Beardsley (1993), Temporal and spatial variability of volume transport of the Kuroshio in the East China Sea, *Deep Sea Res., Part I*, 40, 583–605.

Ito, T., O. Togawa, M. Ohnish, Y. Isoda, T. Nakayama, S. Shima, H. Kuroda, M. Iwahashio, and C. Sato (2003), Variation of velocity and volume transport of the Tsugaru Warm Current in the winter of 1999–2000, *Geophys. Res. Lett.*, 30(13), 1678, doi:10.1029/2003GL017522.

Jochum, M., and R. Murtugudde (2006), Temperature advection by tropical instability waves, *J. Phys. Oceanogr.*, 36, 592–605.

Jochum, M., P. Malanotte-Rizzoli, and A. Busalacchi (2004), Tropical instability waves in the Atlantic Ocean, *Ocean Modell.*, 7, 145–163.

Jochum, M., R. Murtugudde, R. Ferrari, and P. Malanotte-Rizzoli (2005), The impact of horizontal resolution on the equatorial mixed layer heat budget in ocean general circulation models, *J. Clim.*, 18, 841–851.

Jochum, M., M. F. Cronin, W. S. Kessler, and D. Shea (2007), Observed horizontal temperature advection by tropical instability waves, *Geophys. Res. Lett.*, 34, L09604, doi:10.1029/2007GL029416.

Johns, W., T. Shay, and D. Watts (1995), Gulfstream structure, transport and circulation near 68W., *J. Geophys. Res.*, 100, 817–838.

Johns, W. E., T. N. Lee, D. Zhang, R. Zantopp, C.-T. Liu, and Y. Yang (2001), The Kuroshio east of Taiwan: Moored transport observations from the WOCE PCM-1 array, *J. Phys. Oceanogr.*, 31, 1031–1053.

Johnson, G., M. McPhaden, and E. Firing (2001), Equatorial Pacific ocean horizontal velocity, divergence and upwelling, *J. Phys. Oceanogr.*, 31, 839–849.

Karcher, M. J., R. Gerdes, F. Kauker, and C. Koberle (2003), Arctic warming: Evolution and spreading of the 1990s warm event in the Nordic seas and the Arctic Ocean, *J. Geophys. Res.*, 108(C2), 3034, doi:10.1029/2001JC001265.

Kawai, H. (1972), Hydrography of the Kuroshio Extension, in *Kuroshio: Its Physical Aspects*, edited by H. Stommel and K. Yoshida, pp. 235–354, University of Tokyo Press, Tokyo.

Killworth, P. D., D. Stainforth, D. J. Webb, and S. M. Paterson (1991), The development of a free-surface Bryan-Cox-Semtner ocean model, *J. Phys. Oceanogr.*, 21, 1333–1348.

Kim, K., S. J. Lyu, Y.-G. Kim, B. H. Choi, K. Taira, H. T. Perkins, W. J. Teague, and J. W. Book (2004), Monitoring volume transport through measurement of cable voltage across the Korea strait, *J. Atmos. Ocean. Technol.*, 21, 671–682.

Kwon, Y.-O., and C. Deser (2007), North Pacific decadal variability in the Community Climate System Model version 2, *J. Clim.*, 20, 2416–2433.

Large, W. G., and G. Danabasoglu (2006), Attribution and impacts of upper-ocean biases in CCSM3, *J. Clim.*, 19, 2325–2346.

Large, W. G., G. Danabasoglu, J. C. McWilliams, P. Gent, and F. O. Bryan (2001), Equatorial circulation of a global ocean climate model with anisotropic horizontal viscosity, *J. Phys. Oceanogr.*, 31, 518–536.

Legeckis, R. (1977), Long waves in the eastern equatorial Pacific ocean: A view from a geostationary satellite, *Science*, 197, 1179–1181.

Lengaigne, M., G. Madec, C. Menkes, and G. Alory (2003), Impact of isopycnal mixing on the tropical ocean circulation, *J. Geophys. Res.*, 108(C11), 3345, doi:10.1029/2002JC001704.

Levitus, S., et al. (1998), World ocean database 1998, *NOAA Atlas NESDIS*, 18, 346 pp.

Lie, H.-J., C.-H. Cho, J.-H. Lee, P. Niller, and J.-H. Hu (1998), Separation of the Kuroshio water and its penetration onto the continental shelf west of Kyushu, *J. Geophys. Res.*, 103, 2963–2976.

Maes, C., G. Madec, and P. Delecluse (1997), Sensitivity of an equatorial Pacific OGCM to the lateral diffusion, *J. Phys. Oceanogr.*, 125, 958–971.

Maslowski, W., D. Marble, W. Walczowski, U. Schauer, J. L. Clement, and A. J. Semtner (2004), On climatological mass, heat, and salt transports through the Barents Sea and Fram Strait from a pan-Arctic coupled ice-ocean model simulation, *J. Geophys. Res.*, 109, C03032, doi:10.1029/2001JC001039.

McCreary, J., P. Lu, and Z. Yu (2002), Dynamics of the Pacific subsurface countercurrents, *J. Phys. Oceanogr.*, 32, 2379–2404.

McWilliams, J. C. (1996), Modeling the oceanic general circulation, *Annu. Rev. Fluid Mech.*, 28, 215–248.

Munk, W. (1950), On the wind-driven ocean circulation, *J. Meteorol.*, 7, 79–93.

Nakamura, H., and A. S. Kazmin (2003), Decadal changes in the North Pacific oceanic frontal zones as revealed in ship and satellite observations, *J. Geophys. Res.*, 108(C3), 3078, doi:10.1029/1999JC000085.

Neale, R. B., J. H. Richter, and M. Jochum (2008), The impact of convection on ENSO: From a delayed oscillator to a series of events, *J. Clim.*, doi:10.1175/2008JCLI2244.1.

Niiler, P. P., N. A. Maximenko, and J. C. McWilliams (2003), Dynamically balanced absolute sea level of the global ocean derived from near-surface velocity observations, *Geophys. Res. Lett.*, 30(22), 2164, doi:10.1029/2003GL018628.

Nonaka, M., H. Nakamura, Y. Tanimoto, T. Kagimoto, and H. Sasaki (2006), Decadal variability in the Kuroshio-Oyashio Extension simulated in an eddy-resolving OGCM, *J. Clim.*, 19, 1970–1989.

Olbers, D., K. Lettmann, and R. Timmermann (2006), Six circumpolar currents - On the forcing of the Antarctic Circumpolar Current by wind and mixing, *Ocean Dyn.*, 57, 12–31.

Palmer, T., and D. A. Mansfield (1984), Response of two atmospheric general circulation models to SST anomalies in the tropical east and west Pacific, *Nature*, 310, 483–488.

Pedlosky, J. (1996), *Ocean Circulation Theory*, Springer, New York.

Pezzi, L. P., and K. J. Richards (2003), Effects of lateral mixing on the mean state and eddy activity of an equatorial ocean, *J. Geophys. Res.*, 108(C12), 3371, doi:10.1029/2003JC001834.

Pickart, R., D. Torres, and R. Clarke (2002), Hydrography of the Labrador Sea during active convection, *J. Phys. Oceanogr.*, 32, 428–457.

Rayner, N. A., et al. (2003), Global analyses of sea surface temperature, sea ice, and night marine air temperature since the late nineteenth century., *J. Geophys. Res.*, 108(D14), 4407, doi:10.1029/2002JD002670.

Reynolds, R., and T. Smith (1994), Improved global SST analyses using optimal interpolation, *J. Clim.*, 7, 929–948.

Roberts, M. J., et al. (2004), Impact of eddy-permitting ocean resolution on control and climate change solution with a coupled GCM, *J. Clim.*, 17, 3–20.

Rudels, B., and H. J. Friedrich (2000), The transformations of Atlantic water in the Arctic Ocean and their significance for the freshwater budget, in *The Freshwater Budget of the Arctic Ocean*, edited by E. L. Lewis, pp. 503–532, Kluwer Acad., Norwell.

Schlosser, P., et al. (1997), The first trans-Arctic C-14 section: Comparison of the mean ages of the deep waters in the Eurasian and Canadian basins of the Arctic Ocean, *Nucl. Instrum. Phys. Res., Sect. B*, 123, 431–437.

Serreze, M. C., M. M. Holland, and J. Stroeve (2007), Perspectives on the Arctic's shrinking sea-ice cover, *Science*, 315, 426, doi:10.1126/science.1139.

Smagorinsky, J. (1963), General circulation experiments with the primitive equations, *Mon. Weather Rev.*, 91, 99–164.

Smagorinsky, J. (1993), *Large Eddy Simulation of Complex Engineering and Geophysical Flows*, Cambridge Univ. Press, New York.

Smith, R. D., and P. R. Gent (2002), Reference manual for the Parallel Ocean Program (POP), ocean component of the Community Climate System Model (CCSM2.0 and 3.0), LANL Tech. Rep. LA-UR-02-2484.

Smith, R. D., and J. C. McWilliams (2003), Anisotropic horizontal viscosity for ocean models, *Ocean Modell.*, 5, 129–156.

Smith, R., M. Maltrud, F. O. Bryan, and M. Hecht (2000), Numerical simulation of the North Atlantic Ocean at 1/10 degree, *J. Phys. Oceanogr.*, 30, 1532–1561.

Solomon, H. (1971), On the representation of isentropic mixing in ocean circulation models, *J. Phys. Oceanogr.*, 1, 233–234.

Steele, R. D., R. Morley, and W. Ermold (2001), PHC: A global ocean hydrography with a high quality Arctic Ocean, *J. Clim.*, 14, 2079–2087.

Sundermeyer, M. A., and J. F. Price (1998), Lateral mixing and the North Atlantic Tracer Release Experiment: Observations and numerical simula-

tions of Lagrangian particles and a passive tracer, *J. Geophys. Res.*, *103*, 21,481–21,497.

Theiss, J. (2004), Equatorward energy cascade, critical latitude, and the predominance of cyclonic vorticies in geostrophic turbulence, *J. Phys. Oceanogr.*, *34*, 1663–1678.

Tsuchiya, M. (1975), Subsurface countercurrents in the eastern equatorial Pacific Ocean, *J. Mar. Res.*, *33* (Suppl.), 145–175.

Visbeck, M., J. Marshall, T. Haine, and M. A. Spall (1997), On the specification of eddy transfer coefficients in coarse ocean resolution models, *J. Phys. Oceanogr.*, *27*, 381–402.

Wajsowicz, R. (1993), A consistent formulation of the anisotropic stress tensor for use in models of the large-scale ocean circulation, *J. Comput. Phys.*, *105*, 333–338.

Weaver, J., and E. Sarachik (1990), On the importance of vertical resolution in certain ocean general circulation models, *J. Phys. Oceanogr.*, *20*, 600–609.

Whitworth, T., and R. Peterson (1985), Volume transport of the Antarctic Circumpolar Current from bottom pressure measurements, *J. Phys. Oceanogr.*, *15*, 810–816.

Zhurbas, V., and I. S. Oh (2003), Lateral diffusivity and Lagrangian scales in the Pacific Ocean as derived from drifter data, *J. Geophys. Res.*, *108*(C5), 3141, doi:10.1029/2002JC001596.

————————————
G. Danabasoglu, M. Holland, M. Jochum, Y.-O. Kwon, and W. G. Large, Oceanography Section, National Center for Atmospheric Research, 1850, Table Mesa Drive, Boulder, CO 80305, USA. (markus@ucar.edu)